https://doi.org/10.5194/acp-2022-194
Preprint. Discussion started: 6 April 2022

Atmospheric Chemistry and Physics Discussions

Chemical properties, sources and size-resolved hygroscopicity of submicron black carbon-containing aerosols in urban Shanghai

Shijie Cui[1], Dan Dan Huang[2], Yangzhou Wu[1,a], Junfeng Wang[1], Fuzhen Shen[1,b], Jiukun Xian[1], Yunjiang Zhang[1], Hongli Wang[2], Cheng Huang[2], Hong Liao[1], Xinlei Ge[1,*]

[1] Jiangsu Key Laboratory of Atmospheric Environment Monitoring and Pollution Control, Collaborative Innovation Center of Atmospheric Environment and Equipment Technology, School of Environmental Science and Engineering, Nanjing University of Information Science and Technology, Nanjing 210044, China

[2] Shanghai Academy of Environmental Sciences, Shanghai 200233, China

[a]now at: Department of Atmospheric Sciences, School of Earth Sciences, Zhejiang University, Hangzhou 310027, PR China

[b]now at: Department of Meteorology, University of Reading, Reading, RG6 6BX, UK

*Corresponding author: Xinlei Ge (Email: caxinra@163.com)

For *Atmospheric Chemistry and Physics*

https://doi.org/10.5194/acp-2022-194
Preprint. Discussion started: 6 April 2022

Atmospheric Chemistry and Physics Discussions

Abstract. Refractory black carbon (*r*BC) aerosols play an important role in air quality and climate change, yet high time-resolved and detailed investigation on the physicochemical properties of *r*BC and its associated coating is still scarce. In this work, we used a laser-only Aerodyne soot particle aerosol mass spectrometer (SP-AMS) to exclusively measure the *r*BC-containing (*r*BCc) particles, and compared their properties with the total non-refractory submicron particles (NR-PM_1) measured in parallel by a high-resolution AMS (HR-AMS) in Shanghai. The observation shows that *r*BC was overall thickly coated with an average mass ratio of coating to *r*BC core (R_{BC}) of ~5.0. However, mass of *r*BC coating species only occupied 19.1% of those in NR-PM_1; sulfate tended to condense preferentially on non-*r*BC particles therefore its portion on *r*BC was only 7.4%, while the majority of primary organic aerosols (POA) were associated with *r*BC (72.7%). Positive matrix factorization reveals that cooking emitted organics did not coat on *r*BC, and a portion of organics coated on *r*BC was from biomass burning which was unidentifiable in NR-PM_1 organics. Small *r*BCc particles were predominantly from traffic, while large-sized ones were often mixed with secondary components and typically had thick coating. During this campaign, sulfate and secondary organic aerosol (SOA) species were generated mainly through daytime photochemical oxidation (SOA formation likely involved with in-situ chemical conversion of traffic-related POA to SOA), while nocturnal heterogeneous formation was dominant for nitrate; we also estimated the average times of 5~19 hours for those secondary species to coat on *r*BC. Particles during a short period that was affected by ship emissions, were characterized with a high vanadium concentration (on average 5.8 ng m^{-3}) and a vanadium/nickel mass ratio of 2.0. Furthermore, the size-resolved hygroscopicity parameter (κ_{rBCc}) of *r*BCc particles was obtained based on its fully chemical characterization, and was parameterized as $\kappa_{rBCc}(x) = 0.29 - 0.14 \times \exp(-0.006 \times x)$ (x is from 150 to 1000 nm). Under critical supersaturations (SS_C) of 0.1% and 0.2%, the D_{50} values were 166 ± 16 and 110 ± 5 nm, respectively, and with 16 ± 3% and 59 ± 4% of *r*BCc in number could be activated into cloud condensation nuclei (CCN). Our findings are valuable to advance the understanding of BC chemistry as well as the effective control of atmospheric BC pollution.

https://doi.org/10.5194/acp-2022-194
Preprint. Discussion started: 6 April 2022


Atmospheric Chemistry and Physics Discussions

1 Introduction

Refractory black carbon (*r*BC) aerosols can directly absorb solar radiation, indirectly change the nature of cloud and alter the albedo of snow or glaciers (Jacobi et al., 2015), resulting in a positive radiative forcing that is second only to carbon dioxide on both regional and global scales (Ramanathan and Carmichael, 2008;Bond et al., 2013). The fresh *r*BC particles produced by incomplete combustion of biomass and fossil fuel tend to be fractal in morphology and can mix with many other components (Peng et al., 2016;Li et al., 2021). After entering into the atmosphere, fresh *r*BC can further externally or internally mix with organic/inorganic species which are primarily emitted or secondarily formed, and such aged *r*BC-containing (*r*BCc) particles (Chen et al., 2017;Lee et al., 2017) might have contrasting chemical properties and morphologies (or mixing states) (Liu et al., 2017a;Lee et al., 2019;Xie et al., 2019). In addition, when *r*BC mixes with hydrophilic materials, its hygroscopicity, cloud condensation nuclei (CCN) activity and size distribution, etc., can be significantly changed, which subsquently affect its atmospheric behavior, impact and lifecycle (Liu et al., 2013;Lambe et al., 2015). Therefore, it is necessary to elucidate the physicochemical characteristics and sources of *r*BC cores and associated coating materials, so as to better understand their influences on climate and air quality.

Chemical composition of ambient *r*BCc particles is largely dependent upon atmospheric conditions and emission sources. In general, the thickness of coating, mass contribution of secondary components (such as sulfate, nitrate and secondary organic aerosol (SOA) species) and oxidation degree of the coated organics of *r*BCc particles, increase with the aging time or oxidation capacity of ambient environment (Cappa et al., 2012;Liu et al., 2015;Wang et al., 2017;Collier et al., 2018;Wang et al., 2019), except in some specific cases that thickly coated *r*BCc might be dominated by primarily emitted particles (such as from biomass burning (Wang et al., 2017)). Recent field observations report that SOA species coated on *r*BC cores could account for 35% and 41% of the total SOA mass near traffic emission sources and in a polluted offshore environment, respectively (Massoli et al., 2012;Massoli et al., 2015). A study of *r*BCc particles in Singapore finds that over 90% of *r*BC derived from local combustion

https://doi.org/10.5194/acp-2022-194
Preprint. Discussion started: 6 April 2022


Atmospheric Chemistry and Physics Discussions

sources (mainly traffic), while 30% of *r*BC was associated with fresh SOA generated under the influences of daytime shipping and industrial emissions (Rivellini et al., 2020).The SOA material concentrated on the surface of *r*BC was found to be chemically different from the SOA that was externally mixed with *r*BC (Lee et al., 2017) in Fontana, California, and another study in Shenzhen, China, reveals that more oxidized SOA preferred to mix with *r*BC due to that abundant transition metals detected on *r*BC cores might act as catalysts to convert less oxidized SOA to more oxidized SOA in aerosol aqueous phase (Cao et al., 2022); the *r*BC could catalyze SO_2 to form sulfate as well, as observed in Beijing (Zhang et al., 2020) and Guangzhou (Zhang et al., 2021), China. Besides SOA, cooking-related OA is found to be externally mixed with *r*BC (Lee et al., 2017;Wang et al., 2019), and a unique biomass burning related OA factor was identified and was only present in *r*BCc rather than non-*r*BC particles during summertime in Beijing (Wang et al., 2020a).

Size distribution of *r*BCc particles is also modulated greatly by their original sources and ageing processes. For example, a study in Shanghai shows a bimodal size distribution of *r*BCc, with a condensation mode dominated by traffic emissions (small core size, thin coating) and a droplet mode including highly aged biomass burning particles (large core size and thick coating) and highly aged traffic particles (small core size and very thick coating) (Gong et al., 2016). Another study in Beijing (Liu et al., 2019) further resolves four size modes of *r*BCc, relevant with traffic (small core, thin coating), coal or biomass burning (moderate coating, both small and large cores), coal combustion (large core, think coating) and secondary process (thick coating, both small and large cores).

Moreover, water uptake and CCN activity of *r*BCc particles can increase with the encapsulation of water-soluble substances such as sulfate, nitrate, and SOA (Liu et al., 2013;Wu et al., 2019). Based on the measured chemical composition of *r*BCc, our previous work has established a method for calculating size-resolved hygroscopicity parameters of *r*BCc (κ_{rBCc}), and determined the CCN activation diameters of *r*BCc particles for given critical supersaturation (SS_C) values (Wu et al., 2019).

Highly time-resolved chemical characterization of *r*BCc particles were seldom

https://doi.org/10.5194/acp-2022-194
Preprint. Discussion started: 6 April 2022


Atmospheric Chemistry and Physics Discussions

reported in China and is still lacking in Shanghai. In this study, we utilized an Aerodyne soot particle aerosol mass spectrometer (SP-AMS) to determine the concentration, composition and size distribution of *r*BCc particles exclusively (technical details in Section 2.1) in urban Shanghai for the first time. We also compared the SP-AMS measurement results with those from a co-located Aerodyne high-resolution time-of-flight aerosol mass spectrometer (HR-AMS), to comprehensively investigate the characteristics of *r*BCc particles. We analyzed κ_{rBCc} and estimated the proportions of activated *r*BCc numbers at given SS_C as well.

2 Experimental methods

2.1 Sampling site and instrumentation

The field measurement was conducted from October 31 to December 2, 2018, during which the instruments were deployed on 8th floor of the building of Shanghai Academy of Environmental Sciences (SAES) (31°10'33.348" N, 121°26'10.978" E). East of the sampling site is a large commercial shopping center, and the site is surrounded by residential areas with two busy arterial roads directly to the east (~450 m) and south (~150 m), respectively (Figure S1 in the supporting information). In addition, the adjacent areas are densely populated with roadside residents, office workers, and market traders, as well as crowds in and out of the Caobao Road Metro station (~100 m). The measurement period was dominated by northeasterly winds, while many international freight companies located on northeastern side of the site, and many freighters were reposing on the Huangpu River. Overall, the sampling site was probably influenced by vehicular emissions, residential activities and the northeast Cargo ship emission plumes, etc.

An Aerodyne SP-AMS and an HR-AMS were operated in parallel during the campaign. The two AMSs shared a same sampling line with a $PM_{2.5}$ cyclone (Model URG-2000-30EN) in front to remove coarse particles. Ambient air pulled through the sampling line was dried using a diffusion dryer filled with silicon gel and was subsequently drawn into both instruments. Due to the transmission efficiency of the inlet lens, both AMSs measured mainly particles of 30-1200 nm (denoted as PM_1).

https://doi.org/10.5194/acp-2022-194
Preprint. Discussion started: 6 April 2022


Atmospheric Chemistry and Physics Discussions

The working principle of SP-AMS has been described in detail previously (Onasch et al., 2012). However, in this work, we used only the intracavity infrared laser vaporizer to selectively measure *r*BCc particles (*r*BC cores and associated coating materials), as *r*BC can absorb 1064 nm laser light. The thermal tungsten vaporizer had to be physically detached otherwise non-*r*BC particles can still be detected as the filament can heat the vaporizer to ~200 °C even if it was turned off. Before sampling, the SP-AMS was tuned and calibrated following the steps described previously (Lee et al., 2015;Willis et al., 2016;Wang et al., 2017). During sampling, due to relatively low *r*BCc mass loadings, the SP-AMS was operated with two mass sensitive V modes (2.5 minutes per cycle), one with a particle time-of-flight (PToF) mode (30 s) and another one (120 s) with a mass spectral mode with mass-to-charge (*m/z*) ratio up to 500. Filtered air was also measured in the middle of campaign (for 60 min) to determine the limits of detection (LOD, three times the standard deviation) of various aerosol species and to adjust the air-influenced mass spectral signals (Zhang et al., 2005).

Before removal of the tungsten heater, the calibrations of ionization efficiency (IE) for nitrate and relative ionization efficiency (RIE) of sulfate were performed by using pure ammonium nitrate and ammonium sulfate particles (Jayne et al., 2000), and the values were assumed to be unchanged throughout the whole campaign (Willis et al., 2016). RIE of *r*BC to nitrate was calibrated by using size-selected (300 nm) BC particles (REGAL 400R pigment black, Cabot Corp.) (Onasch et al., 2012), and the average ratio of C_1^+ to C_3^+ was calculated to be 0.584 to correct the interference on C_1^+ from other organics. RIEs of ammonium, nitrate, sulfate and *r*BC were determined to be 4.53, 1.10, 1.01, and 0.17, respectively, and RIE of organics used the default value of 1.4 (Canagaratna et al., 2007). The size was calibrated by Polystyrene latex (PSL) spheres (100–700 nm) (Duke Scientific Corp., Palo Alto, CA) before the measurement. This study applied a collection efficiency (CE) of 0.5 for SP-AMS.

The co-located HR-AMS (DeCarlo et al., 2006) was used to measure all PM_1 including both *r*BCc and non-*r*BC particles, but it detected only non-refractory species (NR-PM_1 species) as its 600 °C thermal heater is unable to vaporize *r*BC and other refractory components. In addition, mass concentrations of gaseous pollutants, carbon

https://doi.org/10.5194/acp-2022-194
Preprint. Discussion started: 6 April 2022


Atmospheric Chemistry and Physics Discussions

monoxide (CO), ozone (O_3), nitrogen dioxide (NO_2), and sulfur dioxide (SO_2) were measured by the Thermo Scientific analyzers provided by SAES. Meteorological parameters including air temperature (T), relative humidity (RH), wind speed (WS), wind direction (WD) and precipitation, were obtained from Xujiahui Environmental Monitoring Station of Shanghai (31°11'49.1424"N, 121°26'34.44" E)(~2400 m away from the site). The concentrations of particle-phase vanadium (V) and nickel (Ni) that were used to investigate ship influence were measured independently by an Atmospheric heavy metal analyzer (XHAM-2000A, SAIL HERO., China).

2.2 Data analysis

The AMS data (both SP-AMS and HR-AMS) were analyzed using standard ToF-AMS data analysis tool (Squirrel version 1.59D and Pika version 1.19D), based on Igor Pro 6.37 (Wavemetrics, Lake Oswego, OR, USA). The mass concentrations and high resolution mass spectra (HRMS) of *r*BC and coating species (rBC_{CT}) were calculated from high-resolution (HR) fitting of V-mode data. Size distributions of *r*BCc components were determined by the PToF data with unit mass resolution and were scaled to their mass concentrations obtained above. In particular, size distribution of *r*BC was scaled to that of *m/z* 24 (C_2^+) (the scaling factor is *r*BC mass concentration to that of calculated based on its size distribution), because *m/z* 24 as a *r*BC fragment, has least interference from other organic or inorganic species; such treatment was adopted in earlier studies too (Collier et al., 2018;Wang et al., 2019;Wang et al., 2016).

The HR ion fitting of AMS data is able to distinguish various ions and isotopic ions and calculate elemental ratios of organics such as oxygen-to-carbon (O/C), hydrogen-to-carbon (H/C), nitrogen-to-carbon (N/C), and organic mass to organic carbon (OM/OC) ratios, via the original Aiken-ambient (A-A) method (Aiken et al., 2008) and the improved method (I-A) (Canagaratna et al., 2015b). Outcomes of both methods correlated well. Average O/C, H/C, and OM/OC ratios from the I-A method used in this work were 24.9%, 7.3%, and 5.6%, respectively, higher than those from the A-A method.

Furthermore, we performed Positive matrix factorization (PMF) (Paatero and

https://doi.org/10.5194/acp-2022-194
Preprint. Discussion started: 6 April 2022


Atmospheric Chemistry and Physics Discussions

Tapper, 1994) analysis on the HRMS of organics measured by the SP-AMS via the PMF Evaluation Tool (Ulbrich et al., 2009). The PMF solutions were thoroughly evaluated following the protocols documented in Zhang et al. (2011). Finally, a 6-factor solution was chosen as the optimal one. The final result included four primary OA (POA) factors, namely hydrocarbon-like species enriched OA (HOA-rich), *r*BC-enriched OA (*r*BC-rich), biomass burning OA (BBOA), water-soluble hydrocarbon-like species enriched OA (WS-HOA), and two secondary OA (SOA) factors including a less oxidized oxygenated OA (LO-OOA$_{rBC}$), and a more oxidized oxygenated OA (MO-OOA$_{rBC}$) (Key diagnostic plots in Fig. S2). The HR-AMS data were processed in a similar way, and four factors of NR-PM$_1$ organics were resolved, including hydrocarbon-related OA (HOA$_{NR\text{-}PM1}$), cooking OA (COA$_{NR\text{-}PM1}$), less oxidized oxygenated OA (LO-OOA$_{NR\text{-}PM1}$), and more oxidized oxygenated OA (MO-OOA$_{NR\text{-}PM1}$) (Mass spectra and time series shown in Fig. S3).

2.3 Calculation of size-resolved hygroscopicity of *r*BCc

The hygroscopicity parameter κ is a single parameter representing the hygroscopicity of particles, calculated based on essentially the chemical composition (Petters and Kreidenweis, 2007). SP-AMS measured size-resolved chemical compositions of *r*BCc can thus lead to size-resolved hygroscopicity of *r*BCc (κ_{rBCc}) (Wu et al., 2019;Hu et al., 2021). This study applied a similar method proposed by Wu et al. (2019) and the critical parameters involved in calculation are detailed in Table S1. The procedures are briefly described here: (1) obtain the matrice of size-resolved mass concentrations of each *r*BCc component from SP-AMS analysis; (2) convert the size-resolved concentration matrice of inorganic ions (SO_4^{2-}, NO_3^- and NH_4^+) to corresponding matrice of inorganic salts (NH_4NO_3, NH_4HSO_4, $(NH_4)_2SO_4$) using a simplified solution of ion pairs (Gysel et al., 2007); (3) convert the size-resolved mass matrice of all components (inorganic salts, OA and *r*BC) to those of size-resolved volume fractions (Gysel et al., 2007;Chang et al., 2010;Wu et al., 2016); (4) combine with previously reported hygroscopic parameters (Gysel et al., 2007;Chang et al., 2010;Wu et al., 2016) to obtain the volumetric contributions of each component to the

https://doi.org/10.5194/acp-2022-194
Preprint. Discussion started: 6 April 2022


Atmospheric Chemistry and Physics Discussions

hygroscopicity of *r*BCc; (5) use the Zdanovskii-Stokes-Robinson (ZSR) rule to derive the size-resolved hygroscopicity of *r*BCc (κ_{rBCc}) (Topping et al., 2005a, b).

3 Results and discussion

3.1 Overview of chemical characteristics of *r*BCc and NR-PM_1 particles

Figure 1 presents the time series of meteorological parameters, concentrations of gaseous pollutants (CO, NO_2, O_3, and SO_2), ship emission tracers (vanadium and nickel), *r*BC and rBC_{CT} species and their mass percentages to the total *r*BCc mass, PMF-resolved OA factors and their corresponding fractional contributions. The sampling period was featured by relatively moderate temperatures and very stagnant conditions with average ($\pm1\sigma$) temperature of 15.3 ± (2.9) °C and wind speed (WS) of 0.16 ± (0.29) m s^{-1}. Calm wind (<0.5 m s^{-1}) dominated most of the sampling days and 42% of sampling time was with near-zero wind, therefore overall influence of WS and WD on surface mass loadings of *r*BCc was insignificant. Yet one should keep in mind that WD can affect *r*BCc sources, and WS in higher altitude might be stronger therefore long-range transport of air pollutants was still possible. The average concentrations of CO, NO_2, O_3, SO_2, V, and Ni were determined to be 0.60 ppm, 29.20 ppt, 27.10 ppt, 1.27 ppt, 4.05 ng m^{-3}, and 3.06 ng m^{-3}, respectively.

The mass loadings of *r*BC and rBC_{CT} ranged from 0.04 to 11.00 μg m^{-3} and 0.37 to 30.47 μg m^{-3} with campaign-mean values (± 1σ) of 0.92 ± (0.81) μg m^{-3} and 4.55 ± (4.40) μg m^{-3}. The coating materials accounted for 83.0% of the total *r*BCc mass, of which organics was the most abundant species (2.54 ± 2.52 μg m^{-3}, 46.0%), followed by nitrate (1.20 ± 1.30 μg m^{-3}, 20.0%), ammonium (0.44 ± 0.40 μg m^{-3}, 9.0%), sulfate (0.30 ± 0.19 μg m^{-3}, 6.0%), and chloride (0.07 ± 0.05 μg m^{-3}, 1.0%). The mass ratio of rBC_{CT} to *r*BC (R_{BC}) ranged from 2.2 to 9.0, with an average of ~5.0 (±1.7). The average R_{BC} was higher than that in California (R_{BC} = 2.3) (Collier et al., 2018) and in Shenzhen (R_{BC} = 2.5)(Cao et al., 2022), lower than that in Tibetan Plateau (R_{BC}=7.7) (Wang et al., 2017) and similar to that in Beijing (R_{BC}=5.0) (Wang et al., 2019), suggesting *r*BC was relatively thickly coated throughout the campaign. Correlation between *r*BC and rBC_{CT} was moderate (Pearson's r^2=0.58). Correlation coefficients (r^2) of chloride, nitrate,

https://doi.org/10.5194/acp-2022-194
Preprint. Discussion started: 6 April 2022


Atmospheric Chemistry and Physics Discussions

sulfate and organics with *r*BC were 0.52, 0.75, 0.51 and 0.53, respectively, suggesting variability of sources among different coating components.

Figure 2 compares the campaign-averaged diurnal patterns of rBC_C and NR-PM_1 species, chemical compositions of *r*BCc and NR-PM_1, and mass ratios of the species coated on *r*BC to those of NR-PM_1. We found that the diurnal variations of nitrate, sulfate, ammonium, chloride were very similar (r^2>0.86) between the two particle groups, while apparent difference was found for *r*BCc organics with a much obvious morning rush hour peak. The results indicate that the formation processes of inorganic salts coated on *r*BC were similar to those uncoated on *r*BC, but there were large difference regarding sources/processes existed for organics. For *r*BC itself, the diurnal cycle presented clearly a morning peak and an evening peak, likely relevant with rush hour traffic emissions (CO showed similar pattern). On the contrary, R_{BC} had a minimum in the morning and dropped to a low level in later afternoon, probably due to influence from traffic-emitted fresh and barely coated *r*BC particles (details in Section 3.2.1).

Distributions of species between *r*BCc and non-*r*BC particles were also different, leading to different chemical compositions (Figs. 2g and 2h). Sulfate tended to preferentially condense on non-*r*BC particles, as its mass contribution to total *r*BCc mass was only 6.5%, while its contribution to total NR-PM_1 was 17.6%. Apportionment of nitrate between *r*BCc and non-*r*BC particles was about even as it both occupied ~26% of the total *r*BCc and NR-PM_1 masses. Organics occupied 55.9% of *r*BCc mass, larger than it in NR-PM_1 (43.7%), due to that primary OA species preferentially associated with *r*BC. Such result is similar to that observed in winter in Beijing but contrary to the result that SOA was more abundant in *r*BCc in Shenzhen (Cao et al., 2022).

On average, rBC_C accounted for 19.1% of the total NR-PM_1 mass loading (21.61 ± 15.80 μg m^{-3})(Fig. 2i), comparable to that in Fontana, California (Lee et al., 2017). The finding reveals that significant fractions of aerosol species were externally mixed with *r*BC. Individually, sulfate captured by *r*BC only represented 7.4% of NR-PM_1 sulfate, similar to the eariler results (Lee et al., 2017;Wang et al., 2020a;Cao et al.,

https://doi.org/10.5194/acp-2022-194
Preprint. Discussion started: 6 April 2022


Atmospheric Chemistry and Physics Discussions

2022); mass fractions of *r*BCc nitrate (20.1%) and chloride (20.4%) in NR-PM_1 were similar to the portion of total *r*BC_C (19.1%), while the fraction of organics was higher (26.1%). The relatively high ratio of organics was attributed to the fact that majority of POA species were coated on *r*BC (average ratio of 72.7%), while *r*BC-related SOA was 21.8 % of the total. Note the *r*BCc POA here included all four POA factors, and $COA_{NR\text{-}PM1}$ did not coat on *r*BC thus was not included in the calculation.

3.2 Distinctive sources of OA in *r*BCc and in NR-PM_1

As shown previously, source apportionment results of OA in *r*BCc and NR-PM_1 were different. This section discusses in details the characteristics of OA sources in *r*BCc and in bulk NR-PM_1.

3.2.1 Source apportionment of OA in *r*BCc

Figure 3 shows the HRMS and temporal variations of the six OA factors resolved from PMF analysis of *r*BCc organics. Note the PMF analysis included *r*BC signals (i.e., C_x^+ ions) to aid identification of different factors, yet calculations of elemental ratios of these OA factors did not include C_x^+ ions in order to explicitly explore the properties of organic coating. The HRMS of HOA-rich and *r*BC-rich were similar to the OA previously reported in urban environments near traffic emissions and/or in gasoline/diesel vehicle exhaust (Massoli et al., 2012;Lee et al., 2015;Enroth et al., 2016;Saarikoski et al., 2016;Willis et al., 2016;Lee et al., 2017), therefore both factors were traffic-related. The HOA-rich mass spectrum was featured by intense hydrocarbon ion series (i.e., $C_nH_{2n+1}^+$ and $C_nH_{2n-1}^+$ ions in Fig. 3c), and a lowest O/C ratio of 0.07. Mass fraction of *r*BC signals (i.e., C_n^+ ions, such as *m/z* 12, 24, 36, 48, and 60, etc.) in HOA-rich was 8.1%. Mass spectrum of *r*BC-rich factor had remarkable contribution from *r*BC (24.2%). Beside C_n^+ ions, the *r*BC-rich factor contained more oxygenated organic fragments and presented a higher O/C ratio of 0.21 than that of HOA-rich, similar to previous studies (Willis et al., 2016;Lee et al., 2017). This result is reasonable as previous studies (Corbin et al., 2014;Malmborg et al., 2017) found that refractory organics could generate oxygenated ion fragments (such as CO^+ and CO_2^+ derived from oxygenated species on soot surface or inside soot nanostructure). HOA-rich factor

https://doi.org/10.5194/acp-2022-194
Preprint. Discussion started: 6 April 2022


Atmospheric Chemistry and Physics Discussions

correlated very well with the common AMS tracer of vehicular OA, $C_4H_9^+$ (r=0.95, Fig. 3i), while rBC-rich factor did match the variation of rBC well (r=0.90, Fig. 3g). Since diesel combustion often releases more rBC than that of gasoline, it is likely that the rBC-rich factor is representative of diesel vehicle exhaust while HOA-rich factor represents gasoline combustion emissions. This result demonstrates that laser-only SP-AMS is capable of distinguishing diesel and gasoline burning particles which typically cannot be separated by other AMS measurements. Further verification should be subject of future work.

In this work, a multiple linear regression for the three-dimension size-resolved mass spectra according to the method provided in Ulbrich et al. (2012) was used to resolve the average size distributions of six OA factors. The diagnostic plots are shown in Fig. 4. Overall, the lumped size distribution of six OA factor could reproduce well that of total OA (except for a few size bins, most deviations are within 10%). Correlation between measured and reconstructed OA of all size bins was very tight with r of 0.99 and a slope of 0.97, indicating the robustness of the regressed size distributions of all OA factors. The results together with size distributions of rBCc components, and corresponding mass fractional contributions of different components in all size bins are illustrated in Fig. 5. The average HOA-rich size distribution peaked around 150 nm (D_{va}, vacuum aerodynamic diameter), generally matching with previously reported size distribution of HOA (Sun et al., 2012;Ulbrich et al., 2012;Zhou et al., 2016). Interestingly, size distribution of rBC-rich factor presented two modes, with one peaking ~260 nm, and a more pronounced one peaking ~580 nm (Fig. 5a).

The BBOA was identified owing to its obviously higher signals of $C_2H_4O_2^+$ (2.03%) and $C_3H_5O_2^+$ (1.62%) than those in other factors, as these two ions are well-known AMS fragments of the biomass burning tracer, levoglucosan (Mohr et al., 2009;Cubison et al., 2011). In addition, the time series of BBOA correlated particularly tightly with both marker ions (r of 0.86 and 0.80, respectively); it in fact also correlated well with K^+ (r=0.79), another tracer of biomass burning emission. The O/C and H/C ratios of BBOA were 0.12 and 1.78, and C_n^+ ions accounted for 9.1% of BBOA, all suggesting that the factor was fresh and might be co-emitted with rBC. A relatively high N/C ratio (0.033)

https://doi.org/10.5194/acp-2022-194
Preprint. Discussion started: 6 April 2022


Atmospheric Chemistry and Physics Discussions

was found for BBOA, which could be attributed to the large amounts of nitrogen-containing organic species enriched in biomass burning OA (Laskin et al., 2009). In addition, the size distribution of BBOA (Fig. 5a) (peak size ~500 nm) was similar to that of biomass burning BC-containing particles obtained using single particle mass spectrometry in Shanghai (Gong et al., 2016).

The PMF analysis deconvoluted a unique OA factor coated on *r*BC, namely WS-HOA. Firstly, the WS-HOA mass spectrum had a series of hydrocarbon ion fragments and its time series correlated well with them (e.g., *r* of 0.90 and 0.92 for WS-HOA *vs*. $C_4H_7^+$ and $C_4H_9^+$, respectively). Secondly, this factor correlated the best (r=0.57) with aerosol liquid water content (ALWC) (Fig. 3j) compared with the other five OA factors (all r<0.2). Thirdly, a previous study (Ye et al., 2017) that investigated specially the water-soluble fraction of OA via PMF analysis, separated also a HOA factor that contained significant nitrogen-containing organic fragments, with a highest N/C ratio among all other factors, and correlated well those nitrogenated fragments. The WS-HOA defined here showed similar characteristics with the highest N/C (0.037) among all factors and tight correlations with nitrogen-containing fragments (r>0.80). At last, although WS-HOA had a relatively high O/C (0.31) with remarkable contributions from $C_2H_3O^+$ and CO_2^+, yet its correlations with these two ions were in fact not strong (*r* of 0.46 and 0.44, respectively); and WS-HOA had the least fraction of *r*BC fragments (0.9%) (note *r*BC is hydrophobic), even less than the two SOAs (Fig. 3d). Both results suggest that this factor is a collection of water-soluble primary OA species. The peak of WS-HOA size distribution was ~150 nm, close to that of HOA-rich (Figs. 5a). Aqueous-phase processed SOA (aqSOA) were typically with very high O/C ratio (Xu et al., 2019), and size distribution of aqSOA often presented a droplet mode, peaking in relatively large sizes (such as 500~600 nm)(Gilardoni et al., 2016;Wang et al., 2021;Ge et al., 2012). Therefore, the moderate O/C (0.31) and small mode size of WS-HOA again manifest it was not from aqueous-phase reactions but more likely the water-soluble fraction of POA.

The PMF analyses separated two SOA factors, LO-OOA$_{rBC}$ and MO-OOA$_{rBC}$. Mass spectral features of the two SOAs were consistent with previous studies: The LO-

https://doi.org/10.5194/acp-2022-194
Preprint. Discussion started: 6 April 2022


Atmospheric Chemistry and Physics Discussions

380 OOA$_{rBC}$ was rich in $C_xH_yO_1^+$ ions (38.7%) (such as $C_2H_3O^+$ at *m/z* 43) but with less
381 contribution from $C_xH_yO_2^+$ ions (7.6%) and an overall moderate O/C (0.25), while MO-
382 OOA$_{rBC}$ had much more contribution from $C_xH_yO_2^+$ ion family (22.7%) (such as CO_2^+
383 at *m/z* 44) and $C_xH_yO_1^+$ ions (44.7%), with a high O/C ratio (0.56). In addition, LO-
384 OOA$_{rBC}$ correlated better with nitrate (r=0.83) than it with sulfate (r=0.69), while the
385 correlation between MO-OOA$_{rBC}$ and sulfate (r=0.84) is better than it with nitrate
386 (r=0.76). Size distributions of the two SOAs were also in accord with their secondary
387 behaviors, both accumulating at larger sizes (~450 nm for LO-OOA$_{rBC}$, and a bit larger
388 mode size of ~500 nm for MO-OOA$_{rBC}$), in agreement with previous observations (Sun
389 et al., 2012;Ulbrich et al., 2012;Zhou et al., 2016).

390 In total, traffic-related POA (sum of HOA-rich, *r*BC-rich and WS-HOA) was the
391 most abundant source of *r*BCc organics (39.1%); BBOA occupied ~18.4%; the
392 contributions of two SOAs were on par with each other (20.2% for LO-OOA$_{rBC}$, and
393 22.3% for MO-OOA$_{rBC}$) (Fig. 2g). Among traffic POA, gasoline derived HOA-rich
394 factor outweighed the diesel derived *r*BC-rich factor (11.4% *vs.* 6.3% of the total *r*BCc).
395 Contributions of different factors varied greatly for different sizes of *r*BCc particles
396 (Fig. 5b). Small-sized particles were overwhelmingly dominated by traffic POA; SOA
397 contributions increased with increase of size, and dominated over POA for 300-800 nm
398 ones; contribution of BBOA was also relative larger for 300-800 nm than for other-
399 sized ones; the very large particles (800-1000 nm) were found to be affected mainly by
400 traffic POA in this work. Correspondingly, for the total *r*BCc particles, *r*BC cores
401 peaked at ~170 nm, while other secondary inorganic components, behaving like SOA
402 factors, all peaked at a big size (~550 nm) (Fig. 5c) and their mass percentages were
403 also large for large-sized particles (Fig. 5d).

404 Figure 6a further demonstrates the changes of mass fractions of each *r*BCc
405 component as a function of R_{BC}. R_{BC} is a proxy of coating thickness. It was found that
406 the thinly coated *r*BCc (R_{BC}<3) were dominated (up to ~80%) by traffic-related POA.
407 With the increase of R_{BC}, contribution of secondary components increased gradually,
408 especially the two SOAs and nitrate (sulfate showed little changes across the whole R_{BC}
409 range); SOA and nitrate contributions reached 40.2% and 31.3% at R_{BC} = 8, respectively.

https://doi.org/10.5194/acp-2022-194
Preprint. Discussion started: 6 April 2022


Atmospheric Chemistry and Physics Discussions

Accordingly, the oxidation degree (OSc = 2*O/C-H/C) (Kroll et al., 2011) of coated organics increased with R_{BC}. In Fig. 6b, we presented the mass contributions of OA factors to the *r*BC mass at different R_{BC} values. The *r*BC was as expected, predominantly associated with POA (from 94% at R_{BC}<2 to 66% at R_{BC} >8), similar to those from Fontana (Lee et al., 2017). Contribution of *r*BC-rich factor decreased obviously, and those of SOA factors increased with R_{BC}. The contributions of HOA-rich, WS-HOA and BBOA factors changed little.

3.2.2 Comparisons with NR-PM$_1$ organics

As shown in Fig. S3, PMF analysis separated four OA factor for NR-PM$_1$ organics. Two SOA factors (LO-OOA and MO-OOA) were resolved for both *r*BCc and NR-PM$_1$, and their contributions to them were also close (Figs. 2g and 2h). Correlations of time series between the two LO-OOA factors and between the two MO-OOA factors were also tight (*r* of 0.94 and 0.90, respectively), indicating similar formation processes for each SOA. But, of course, the SOAs from *r*BCc and from NR-PM$_1$ were not entirely the same, as later ones had higher O/C ratios (0.52 of LO-OOA$_{NR\text{-}PM1}$ and 0.62 of MO-OOA$_{NR\text{-}PM1}$). On average, the portion of LO-OOA coated on *r*BC took up 21.6% mass of LO-OOA in total NR-PM$_1$, and the portion was 26.0% for MO-OOA. This result suggests that there were some but not big differences regarding the partitioning of LO-OOA and MO-OOA onto *r*BCc and non-*r*BC particles.

Compared with SOAs, source apportionment results of POA were quite distinct. Firstly, there was only one HOA factor resolved for NR-PM$_1$, while three HOA factors were separated for *r*BCc. Note the *r*BC-rich and WS-HOA factors occupied merely 3.1% and 2.1% of NR-PM$_1$ OA mass, respectively, probably the cause that they were not identified in NR-PM$_1$ OA. Nevertheless, mass loadings of the sum of HOA-rich, *r*BC-rich and WS-HOA factors (termed as HOA$_{rBC}$) agreed quite well with that of HOA$_{NR\text{-}PM1}$ (r=0.95) (Fig. 7a), verifying both source apportionment results. And, HOA$_{rBC}$ took up 63.7% of HOA$_{NR\text{-}PM1}$, while previous studies reported that 81% (Massoli et al., 2012) and 87 % (Massoli et al., 2015) of HOA were associated with *r*BC. These results imply that HOA species in NR-PM$_1$ were largely internally mixed

https://doi.org/10.5194/acp-2022-194
Preprint. Discussion started: 6 April 2022


Atmospheric Chemistry and Physics Discussions

with *r*BC affected by vehicular emissions. Secondly, $COA_{NR\text{-}PM1}$ was only identified in NR-PM_1 OA. AMS-resolved $COA_{NR\text{-}PM1}$ is mainly from cooking oil and food itself, therefore it negligibly internally mixes with *r*BC. This result is consistent with previous observations (Lee et al., 2015;Willis et al., 2016;Lee et al., 2017;Collier et al., 2018). At last, BBOA was identified in *r*BCc OA but not in NR-PM_1 OA. One plausible reason was that the BBOA mass contribution was minor (equivalent to <5% of NR-PM_1 OA mass); another speculation is that laser only SP-AMS can detect refractory species that HR-AMS cannot, some of them might be originated from biomass burning (Wang et al., 2020a).

Diurnal cycles of the POA and SOA factors from both PMF analyses are compared in Figs. 7b and 7c. The diurnal pattern of stacked HOA_{rBC} indeed agreed with that of $HOA_{NR\text{-}PM1}$, both with two peaks in the morning and evening rush hours, and, the patterns of *r*BC-rich, HOA-rich, and WS-HOA factors showed similar behaviors individually (Fig. 7b). The diurnal variation of $COA_{NR\text{-}PM1}$ had pronounced peaks during lunch and dinner times, and its percentage in NR-PM_1 OA reached 54% at night. Diurnal patterns of two LO-OOA factors were somewhat different (r=0.35). LO-OOA_{rBC} has a major peak in the afternoon, while though LO-$OOA_{NR\text{-}PM1}$ concentration rose in the afternoon too but peaked in early evening (~8 pm). The daily variations of two MO-OOA factors were similar (r=0.83), both peaking at 16:00. The afternoon increases of both SOAs indicate an important role of photochemical reactions, yet differences in formation mechanisms, volatilities and partitioning behaviors of SOA products could lead to diversities of their diurnal patterns and HRMS.

3.3 Evolution and formation *r*BCc components

3.3.1 Behaviors of *r*BC cores

Size distribution of *r*BC cores shown in Fig. 5c was relatively wide. Beside the main peak at ~170 nm, it extended significantly into large sizes and had a small peak at ~550 nm, which was close to the peak of secondary components. With results shown in Fig. 5a, we found that small *r*BC cores were often thinly coated, while thickly coated *r*BCc particle were often highly aged and a portion of them also had large-sized *r*BC

https://doi.org/10.5194/acp-2022-194
Preprint. Discussion started: 6 April 2022


Atmospheric Chemistry and Physics Discussions

cores. This result is likely owing to that oxidation of *r*BC-bounded organics and/or condensation of secondary species onto *r*BC surface can induce restructuring of soot aggregates to form compact and large cores (Chen et al., 2018;Chen et al., 2016). Such phenomenon is in line with earlier studies (Liu et al., 2019;Gong et al., 2016). We further show the image plot of size distributions of *r*BC at different R_{BC} in Fig. S5a. It can be found that the *r*BC mass in a large part concentrated in particles with R_{BC} of 5-8, and there was indeed a significant portion of *r*BC appearing in large size range (400-800 nm) with very thick coating (R_{BC} of 8-9).

3.3.2 Formation of inorganic salts

Sulfate and nitrate both peaked at a big size ~550 nm (Fig. 5c) and were mainly associated with thickly coated *r*BCc (R_{BC}>6, Figs. S5d and S5e). To investigate the impacts of photochemistry and aqueous/heterogeneous chemistry on the formation of rBC_{CT} species, we plotted the image plots of size distributions of nitrate, sulfate and organics versus O_X ($O_3 + NO_2$) and relative humidity (RH) in Fig. 8. Here O_X is used as a proxy of photochemical activity (Xu et al., 2017), and RH is an indicator of aqueous reactions (Wu et al., 2018). Nitrate significantly concentrated in 65-100 ppb O_X range but there was a weak accumulation in low O_X as well (Fig. 8a), while in Fig. 8d, nitrate had a prominent hotspot in RH>85%. Generally, both strong photochemical activity and high RH could promote nitrate formation. For sulfate, although the distribution was scattered due to low level of mass loadings, high Ox level seemed to favor sulfate formation (Fig. 8b); sulfate was scattered in the whole RH range and there were some enhancements at high RH (>80%) but was much less clear-cut (Fig. 8e). Therefore aqueous-phase production of sulfate was not important in this campaign.

We further calculated the sulfur oxidation ratio (SOR) and nitrogen oxidation ratio (NOR) (Xu et al., 2014), and plotted their variations against O_X and RH in Figs. 9a and 9e, respectively. The NOR rose substantially at O_X >60 ppb but showed no increase at O_X < 60 ppb, while it increased continuously with RH. Mass ratio of nitrate to *r*BC stayed at a high level during nighttime when RH was high as well (overall diurnal trend of NO_3^-/*r*BC was similar to that of RH, see Figs. S6a and S6d). This result indicates a

https://doi.org/10.5194/acp-2022-194
Preprint. Discussion started: 6 April 2022


Atmospheric Chemistry and Physics Discussions

likely more important role of nocturnal nitrate formation (N_2O_5 hydrolysis) (Pathak et al., 2011) (Sun et al., 2011) than photochemical production of nitrate during this campaign; moreover, low temperature and high RH favor nitrate partitioning into the particle phase during nighttime too (Gao et al., 2011). For sulfate, The SOR increased with O_X while it increased with RH under relatively dry conditions (<60%) but decreased with RH when RH>60%. This result, on the other hand, highlights that photochemical production is more important than aqueous/heterogenous formation for sulfate. In addition, mass ratios of sulfate to *r*BC were enhanced remarkably during daytime and peaked in the afternoon (Fig. S6e), supporting the key role of photochemical formation of sulfate. Sulfate precursor SO_2 was at a high level during daytime too. The main formation pathway of sulfate is strikingly different from that observed in winter Nanjing (Wu et al., 2018), suggesting significant seasonal variability of sulfate formation even in the same region.

3.3.3 Evolution of organics

Organics had a broad average size distribution (Fig. 5c), but unlike *r*BC, its main peak appeared at 500~600 nm. Figure S5b shows that the majority of organics partitioned in *r*BCc with R_{BC} of 5.0-9.0 and wide size coverage (300-800 nm). Regarding its dependences on O_X and RH, it mainly accumulated at O_X>70 ppb (Fig. 8c) and very high RH (~90%) (Fig. 8f). Consistently, O/C ratio and OSc both peaked in the afternoon (Fig. S6b), all suggesting a critical role of photochemistry in affecting the behavior of organics.

Figure 9 illustrates the mass ratios of each OA factor to *r*BC varying with O_X and RH. Mass ratios of all four POA factors generally presented decreasing trends (despite some fluctuations) against O_X (Fig. 9b), and the total POA_{rBC} showed evident decrease with increase of O_X (Fig. 9d). Instead, both $LO\text{-}OOA_{rBC}$ and $MO\text{-}OOA_{rBC}$, as well as their sum (SOA_{rBC}) increased continuously with O_X (Figs. 9c and 9d). This result proves that photochemical oxidation contributed significantly to both $LO\text{-}OOA_{rBC}$ and $MO\text{-}OOA_{rBC}$ formations. Comparatively, decreases of POA_{rBC} perhaps point to its reaction loss upon photochemical oxidation. With regard to RH, besides WS-HOA, the other

https://doi.org/10.5194/acp-2022-194
Preprint. Discussion started: 6 April 2022


Atmospheric Chemistry and Physics Discussions

three POA_{rBC} factors showed almost no dependences on RH (Fig. 9f); note the increase of WS-HOA with RH did not indicate the aqueous production of WS-HOA (see discussion in Section 3.2.1), but a result of enhanced dissolution with increase of moisture. Overall small increase of POA_{rBC} (Fig. 9h) with RH then mainly attributed to WS-HOA. Contrary to the trends with O_X, mass ratios of two SOA factors as well as the total SOA to *r*BC went down with increase of RH (Figs. 9g and 9h), indicating a trivial role of aqueous/heterogenous oxidation for the SOA coated on *r*BC observed during this campaign.

The aging of OA is generally characterized by the increase of O/C and decrease of H/C (Ng et al., 2011;Zhao et al., 2019).The different aging pathways of OA follow different slopes in the Van Krevelen (VK) diagram (Heald et al., 2010). For example, addition of only one oxygen atom to the carbon skeleton results in a slope equal to 0, while replacement of the hydrogen atom with a carboxylic acid group (−COOH) results in a slope of −1 without fragmentation (C-C bond breaking), and −0.5 with fragmentation (Heald et al., 2010;Ng et al., 2011;Zhao et al., 2019). As presented in Fig. 10a, fitting of all OA data yielded a slope of −0.96, very close to −1, suggesting that OA ageing process resembled the hydrogen substitution with a –COOH group (carboxylation). Interestingly, the four OA factors (HOA-rich, WS-HOA, $LO\text{-}OOA_{rBC}$ and $MO\text{-}OOA_{rBC}$) aligned almost in a straight line with a slope of −0.77 (Fig. 10a), also close to −1. Figure S7 further reveals that there was a strong anti-correlation between mass fractions of sum of HOA-rich and WS-HOA and sum of $LO\text{-}OOA_{rBC}$ and $MO\text{-}OOA_{rBC}$ (r=−0.97); the slope of fitted line was −0.86. All these results suggest that OA evolution may contain a channel of photochemical transformations from HOA-rich and WS-HOA to $LO\text{-}OOA_{rBC}$ and then to $MO\text{-}OOA_{rBC}$. This result is also in line with the observed decrease of POA_{rBC} and increase of SOA_{rBC} against O_X.

CHO^+, CHO_2^+ and $C_2H_2O_2^+$ are the AMS tracer ions for carbonyl, carboxylic acid and glyoxal, respectively (Wang et al., 2020b;Canagaratna et al., 2015a;Yu et al., 2014). Mass fractions of these three fragment ions presented decreasing trends (or no clear trends) against RH (Fig. S8), suggesting again that aqueous processing is not an important pathway in OA evolution during this campaign. Conversely, fractional

https://doi.org/10.5194/acp-2022-194
Preprint. Discussion started: 6 April 2022


Atmospheric Chemistry and Physics Discussions

560 contributions of these three ions presented increasing trends versus O_X, supporting the
561 dominance of photochemical oxidation pathway (Figs. 10b-d). Figures 10e-g show the
562 scatter plots of H/C versus O/C at different O_X concentrations. The regressed slope was
563 −1.03 for low O_X (<60 ppb) conditions (Fig. 10e), indicating that the OA aging at low
564 O_X level is mainly analogue to the carboxylation process. This result corresponds
565 precisely to the fact that mass fractions of CHO_2^+ and $C_2H_2O_2^+$ increased gradually with
566 O_X at low O_X, whereas that of CHO^+ remained essentially unchanged (Figs. 10e-g). The
567 fitted slope was −1.14 for moderate O_X conditions (60-80 ppb), and it changed to −0.43
568 for high O_X level (>80 ppb) but correlation became weaker (r=−0.57). This result
569 implies that the OA evolution under high O_X conditions might include oxidations by
570 the additions of alcohols, peroxides and carboxylation. In all, the evolution of *r*BCc OA
571 in Shanghai during this campaign is governed by photochemistry rather than aqueous
572 chemistry, but with different oxidation pathways at different O_X levels.
573
574 **3.3.4 Coating time of secondary species onto *r*BC**
575 Although the *r*BCc organics was dominated by primary sources (Fig. 2g), the
576 diurnal variations of OSc, O/C and H/C of the total organics, were controlled
577 predominantly by the two SOA factors. Correlations between the diurnal cycles of MO-
578 OOA_{rBC}/*r*BC and OSc were extremely well (r=0.97 with OS_C and r=0.98 with O/C),
579 and those of LO-OOA/*r*BC were also tight (r=0.91 with OS_C and r=0.92 with O/C).
580 The correlations with LO-OOA_{rBC} were a bit weaker than those of MO-OOA_{rBC},
581 indicating that MO-OOA_{rBC} was probably the final products and was more important
582 in governing the overall oxidation level of organic coating. Figure 11a depicts the
583 diurnal variations of SOA_{rBC}/*r*BC and POA_{rBC}/*r*BC. Diurnal variations of POA_{rBC}/*r*BC
584 and *r*BC were overall similar, while the daily pattern of SOA_{rBC}/*r*BC was almost
585 opposite to that of *r*BC. This result likely indicates that most POA_{rBC} species were co-
586 emitted and coated on *r*BC cores originally, therefore the coating process during *r*BCc
587 lifecycle was mainly relevant with SOA species rather than POA species. This process
588 is mainly through photochemical reactions, including in-situ oxidation of originally
589 coated POA species (for example, oxidation of HOA-rich plus WS-HOA to LO-

https://doi.org/10.5194/acp-2022-194
Preprint. Discussion started: 6 April 2022


Atmospheric Chemistry and Physics Discussions

590 OOA_{rBC}, then to $MO\text{-}OOA_{rBC}$), and partitioning of secondary species formed in gas-
591 phase reactions onto *r*BC surface. In addition, sulfate and nitrate were both secondarily
592 formed, but sulfate was dominated by photochemical production while nitrate was
593 governed by nocturnal heterogenous formation (as discussed in Section 3.3.2); different
594 diurnal patterns of them (Fig. S6) point to different coating processes too.
595 In this regard, we hereby propose a concept of average coating time (ACT), which
596 is used to roughly estimate the timescales required for secondary components coated
597 onto *r*BC. The specific method is listed as follows:
598 1. Move forward the diurnal variation of SA_{rBC}/rBC (SA represents a secondary
599 aerosol species) for *n* hours to get a new SA_{rBC}/rBC diurnal pattern, labelled as
600 "SA_{rBC}/rBC(*r*-*n*h-ahead)". Here, the *r* value is the linear correlation coefficient between
601 the new SA_{rBC}/rBC diurnal pattern with that of *r*BC.
602 2. Choose the best correlation coefficient (*r*-*n*h-ahead), and *n*h corresponds to the
603 ACT for this secondary component.
604 Diurnal patterns of $LO\text{-}OOA_{rBC}/rBC$ and $MO\text{-}OOA_{rBC}/rBC$ are depicted in Fig.
605 11b. They were both opposite to the trend of *r*BC, and they were similar to each other,
606 except that $MO\text{-}OOA_{rBC}/rBC$ peaked hours later in the afternoon, signifying that the
607 $MO\text{-}OOA_{rBC}$ needs longer time to coated on *r*BC than $LO\text{-}OOA_{rBC}$ does, consistent
608 with the fact that $MO\text{-}OOA_{rBC}$ was "more aged". Correspondingly, we obtained an ACT
609 of 7 hours for $MO\text{-}OOA_{rBC}$ (*0.35*-*7*h-ahead) and 5 hours for $LO\text{-}OOA_{rBC}$ (*0.57*-*5*h-
610 ahead) (Fig. 11c) using the method described above. The ACT of sulfate (*0.65*-*7*h-ahead)
611 and nitrate (*0.30*-*19*h-ahead) were 7 and 19 hours, respectively (Fig. 11d). The results
612 suggest that the *r*BC emitted mainly in the morning rush hours requires a few hours to
613 be adequately coated by $LO\text{-}OOA_{rBC}$, $MO\text{-}OOA_{rBC}$ and sulfate, as these three species
614 are mainly produced in the afternoon by photochemical reactions; while photochemical
615 production of nitrate is insignificant, thus *r*BC was coated by nitrate until later night
616 when nitrate was formed efficiently by heterogenous N_2O_5 hydrolysis. Note the best *r*
617 values were not high (for example, 0.35 for $MO\text{-}OOA_{rBC}$ and 0.30 for nitrate), yet the
618 adjusted trends of all secondary components (Figs. 11c and 11d) matched that of *r*BC
619 quite well during 3:00~12:00 (*r* of 0.90, 0.91, 0.84 and 0.84 for $MO\text{-}OOA_{rBC}$, LO-

https://doi.org/10.5194/acp-2022-194
Preprint. Discussion started: 6 April 2022


Atmospheric Chemistry and Physics Discussions

620 OOA$_{rBC}$, sulfate and nitrate, respectively), likely meaning that daytime variations of
621 two SOAs and sulfate were indeed controlled by the coating process while governing
622 factors of their nighttime variations might be complex, and *vice versa* for nitrate.
623
624 **3.4 Size-resolved hygroscopicity of *r*BCc**
625 By using the method in Section 2.3, we calculated the size-resolved hygroscopicity
626 parameters for the total *r*BCc (κ_{rBCc}) and the coatings materials (κ_{CT}) across the whole
627 campaign. The image plots are illustrated in Figs. 12a and b. Generally, large κ_{rBCc} and
628 κ_{CT} values occurred at big particle sizes, and this result was overall similar to that in
629 Nanjing during winter (Wu et al., 2019). We further illustrate the size-resolved κ_{rBCc} as
630 a function of R_{BC} in Fig. 12c. The figure shows that κ_{rBCc} overall became larger with
631 increasing particle size regardless of the coating thickness. However, there were some
632 (though not significant) relatively high κ_{rBCc} values in the range of 80-150 nm (bottom
633 left and bottom right in Fig. 12c).
634 In Figs. 13a and b, we further determined the average size-resolved κ_{rBCc} and κ_{CT}
635 as a function of coated diameter (D_{rBCc}). Both κ_{rBCc} and κ_{CT} values were relatively high
636 at D_{rBCc}<100 nm and presented slight decreases from 100 to 150 nm. This is distinctive
637 from those observed in Nanjing, where κ_{CT} increased with D_{rBCc} from 50 nm (Wu et al.,
638 2019). From Figs. 5b and 5d, it can be seen the *r*BCc with D_{rBCc}<150 nm was dominated
639 by a portion of ammonium and sulfate (8-10%) and organics (~60%), of which organics
640 was dominated by WS-HOA. Such composition explains the relatively high
641 hygroscopicity at D_{rBCc}<150 nm as both ammonium sulfate and WS-HOA are
642 hydrophilic; a slight decrease of the hygroscopicity from 100 to 150 nm D_{rBCc} was also
643 a response of decreased mass contributions of ammonium sulfate and WS-HOA (and
644 increase of hydrophobic HOA-rich contribution).
645 Figures 13a and b provide the fitted exponential functions for the mean κ_{rBCc} and
646 κ_{CT} with D_{rBCc}. The equations are: $\kappa_{rBCc}(x) = 0.29 - 0.14 \times \exp(-0.006 \times x)$ and $\kappa_{CT}(x) = 0.35 - 0.09 \times \exp(-0.003 \times x)$ (x is D_{rBCc}, $150<x<1000$ nm). Here, 0.29 and 0.35 are
647
648 the upper limits of κ_{rBCc} and κ_{CT}, higher than those reported in Nanjing (0.28 and 0.30
649 for κ_{rBCc} and κ_{CT}); yet the increasing rates of κ_{rBCc} and κ_{CT} with D_{rBCc} are 0.14 and 0.09,

https://doi.org/10.5194/acp-2022-194
Preprint. Discussion started: 6 April 2022


Atmospheric Chemistry and Physics Discussions

650 respectively, which are much lower than those from Nanjing (0.35 and 0.27 for κ_{rBCc}
651 and κ_{CT})(Wu et al., 2019). Smaller increased contributions of hydrophilic secondary
652 species from 150 to 1000 nm in Shanghai than those from 100 to 1000 nm in Nanjing
653 are likely the cause of smaller increasing rates of hygroscopicity parameters. In addition,
654 it should be noted that the hygroscopicity is not only determined by the bulk
655 composition, but also affected by the phase state of particles. For instance, a recent
656 study reveals that the hygroscopic growth of phase-separated particles (with ammonium
657 sulfate as cores) can be reduced by the secondary organic shells and is dependent on
658 the thickness of organic coating (Li et al., 2021).
659 The critical supersaturation (SS_C) for a selected dry diameter (D_{rBCc} measured by
660 SP-AMS) of a *r*BCc particle with a hygroscopicity parameter κ_{rBCc}, can be calculated
661 by the "κ-Kohler theory" equation (Petters and Kreidenweis, 2007). Based on the size-
662 resolved κ_{rBCc}, the CCN activation diameter (D_{50}) of particles at a given critical SS_C can
663 be calculated (Wu et al., 2019). Then, by combining the measured *r*BCc number size
664 distribution and the D_{50} value, activation fraction (f_{AC}) of *r*BCc number population (i.e.,
665 the fraction greater than the D_{50}) can be obtained. Figure 13c shows the SS_C as a
666 function of D_{rBCc} for the entire sampling period to obtain the D_{50} at a specific SS_C. The
667 D_{50} values of the *r*BCc particles were determined to be 166 ± 16 nm and 110 ± 5 nm
668 for SS_C of 0.1% and 0.2%, respectively. The two D_{50} values are both smaller than those
669 determined for *r*BCc particle in Nanjing (Wu et al., 2019), likely owing to the presence
670 of WS-HOA in Shanghai. Figure 13d shows the f_{AC} at SS_C of 0.1% (D_{50} of 166 nm) was
671 16 ± 3%, and the f_{AC} at SS_C of 0.2% (D_{50} of 110 nm) was 59 ± 4%.
672
673 **3.5 A case study influenced by ship emissions**
674 **3.5.1 Potential source areas of *r*BCc**
675 To explore the potential geographic origins of *r*BCc at the receptor site, the hybrid
676 single-particle Lagrangian integrated trajectory (HYSPLIT) model (version 4.9) was
677 applied here. Figure 14a shows that the backward trajectories were classified into four
678 air mass clusters, including one long-range transport from northern sea (Cluster1), one
679 long-range transport from northeastern sea (Cluster2), a local one from eastern ports

https://doi.org/10.5194/acp-2022-194
Preprint. Discussion started: 6 April 2022


Atmospheric Chemistry and Physics Discussions

(Cluster3), and one from northwestern inland region (Cluster4). The four clusters occupied 23.8%, 33.8%, 37.3%, and 5.0% of the total trajectories, respectively. It is clear that the sampling period was influenced by offshore air masses in most of the time (95%). Cluster3 had the highest mean *r*BCc concentrations (13.2 ± 10.9 μg m^{-3}) while the mean concentrations of the other three clusters were apparently lower (4.3~5.2 μg m^{-3}). This result is plausible as Cluster3 was the shortest in length therefore was least diluted compared with other three clusters. Average chemical compositions of the *r*BCc from four clusters (Fig. 14b) showed some differences as well: Cluster1 and Cluster2 had higher MO-OOA_{rBC} contributions, possibly owing to the interceptions of more aged SOA species during the long-range transports; While Cluster4 had less MO-OOA_{rBC} but a bit more POA_{rBC} contributions, likely attributing to more primary species emitted in inland regions (similarly, a higher fraction of nitrate was likely because of enhanced NO_2 emissions).

3.5.2 A typical case of *r*BCc affected by ship emissions

Ship emissions are found to have an important impact on the air quality of Shanghai and the Yangtze River Delta (Zhao et al., 2013;Fan et al., 2016;Liu et al., 2017b;Chen et al., 2019). The ship engines usually burn heavy fuel oil (HFO), and vanadium (V) and nickel (Ni) can be adopted as reliable tracers for the ship-emitted particles (Ault et al., 2009;Moldanová et al., 2009;Ault et al., 2010). The long-term variation of Ni/V ratio in ship-emitted particles in Shanghai has been recently reported (Yu et al., 2021). The main conclusion is that Ni/V ratio was close to 0.4 in 2018, while it became to be greater than 2.0 in 2020. Our measurement was carried out in 2018, and we therefore chose a period from November 3 to 5 as a typical case affected by ship emissions (SEP period), since the average Ni/V ratio was ~0.50 and high concentrations of both Ni and V were found. Figure S9 shows the concentration-weighted trajectories (CWT) of ship emission tracers (V, Ni), *r*BC and *r*BC-rich factor during SEP, displaying that these components were mainly from sea. During SEP, the correlation coefficient (*r*) between V(Ni) and *r*BC was 0.69 (0.74), indicating the SEP was indeed impacted by ship emissions.

https://doi.org/10.5194/acp-2022-194
Preprint. Discussion started: 6 April 2022


Atmospheric Chemistry and Physics Discussions

Figure 15 displays the chemical characteristics of *r*BCc and NR-PM_1 components (especially the OA factors), V and Ni, gaseous pollutants and the meteorological parameters during SEP. As a comparison, we also selected a period with no ship emissions with the same time span as SEP (from 0:00 on November 10 to 0:00 on November 12, termed as non-SEP), and a similar plot during non-SEP is presented in Fig. S10. During SEP, the wind was mainly from east, and the average wind speed was ~0.5 m s^{-1} (Fig. 15a); Wusong, Luojing and Waigaoqiao ports located northeast of the sampling site (Fig. S1). Instead, the wind was mainly from north during non-SEP (Fig. S10a). During SEP, the average mass concentrations of V and Ni were 5.8 ng m^{-3} and 2.9 ng m^{-3}, respectively, while those during non-SEP were only 2.9 ng m^{-3} and 2.6 ng m^{-3}. The average mass ratio of V/Ni during SEP was 2.0 in agreement with those reported in ship-influenced PM_1 (Mazzei et al., 2008;Mar et al., 2009), and within the range of 1.9 to 3.5 for domestic HFO (Zhao et al., 2013), while the average ratio of V/Ni (1.1) during non-SEP was outside the range. Moreover, the major air pollutants emitted from ships include nitrogen oxides (NO_x), sulfur oxides (SO_2), carbon monoxide (CO), hydrocarbons and primary/secondary particles (Becagli et al., 2017;Wu et al., 2021). As demonstrated in Fig. 15d and Fig. S10d, SO_2 concentration was overall higher during SEP (10:00-16:00 on November 11 not included); mass loading of NO_2 was higher during the rush hours of non-SEP, but was higher at night (no traffic) during SEP. Mass proportion of sulfate in NR-PM_1 during SEP was also higher than that during non-SEP (21.0% *vs.* 18.7%), but *vice versa* for nitrate (18.8% during SEP *vs.* 25.4% during non-SEP).

We further investigated the dependences of *r*BCc and NR-PM_1 species on V during SEP and non-SEP, as shown in Fig. S11. Here we only used V since Ni level might be influenced by other emission sources, such as refining industry (Jang et al., 2007;Kim et al., 2014) in urban Shanghai, and during non-SEP, Ni still presented a good correlation with *r*BC (r=0.80). During SEP, V concentrations (most of them >4 ng m^{-3}) overall positively correlated with both sulfate and nitrate (except for *r*BCc sulfate) (Fig. S11a). Considering that V concentration was independently measured for all fine particles, a better correlation with total NR-PM_1 sulfate than it with *r*BCc sulfate is

https://doi.org/10.5194/acp-2022-194
Preprint. Discussion started: 6 April 2022


Atmospheric Chemistry and Physics Discussions

740 reasonable. Similarly, V-rich particles had positive correlations with traffic-related OA
741 and LO-OOA no matter in *r*BCc or in total NR-PM_1 (Fig. S11b). Conversely, during
742 non-SEP, particles with low-V content (most of them <4 ng m^{-3}) had no clear links with
743 sulfate, nitrate, POA and SOA species (even anti-correlations for V>2.5 ng m^{-3}) (Figs.
744 S11c and S11d; a detailed comparison of the correlation coefficients of V with OA
745 factors of *r*BCc and NR-PM_1 organics are provided in Table S2). The results above
746 dodemonstrate that during SEP, chemical properties of the particles (both fresh and aged
747 ones) were clearly linked with ship influences.

748 Previous studies (Ault et al., 2009;Ault et al., 2010;Liu et al., 2017b) have shown
749 that the fresh ship-emitted V-rich particles are typically accompanied by high sulfate
750 contribution, while those aged V-containing ship particles are on the other hand with
751 relatively high nitrate contribution. In order to further probe chemical characteristics
752 and evolution processes of particles influenced by ship emissions, we divided SEP into
753 three episodes (i.e., EP1-EP3) (marked in Fig. 15). During EP1, *r*BC content was
754 highest (Fig. 15k) and coating was thinnest (Fig. S12i) indicating the particles were
755 relatively fresh, nevertheless the SOA contents were not low (Figs.15j and 15l), OS_C
756 was moderate (Fig. S12j), sulfate portions in NR-PM_1 and *r*BCc were both the highest
757 (26.5%), and nitrate portion was the lowest (9.8%) among three episodes (Figs.15i and
758 15k). Such composition is not common in other cases, demonstrating it was a specific
759 period impacted by fresh ship emissions. EP2 had the highest mass loadings of V, gas
760 pollutants as well as the lowest planetary boundary layer (PBL) height (~200 meters)
761 (Fig. S12). Mass contributions of nitrate increased and sulfate decreased, and *r*BC
762 content decreased from those during EP1, signifying that the particle population likely
763 contained some aged ship-emitted particles. Of course, particle composition during EP2
764 was also influenced by the formation mechanisms of secondary species: EP2 was
765 mostly during nighttime, therefore photochemical formation of sulfate and SOA were
766 weak (contributions were low as shown in Figs. 15i-l), while nitrate formation was
767 enhanced due to the nocturnal process. During EP3, *r*BC was lowest, sulfate and V were
768 moderate, nitrate and SOA were highest in both *r*BCc and NR-PM_1, OS_C and R_{BC} were
769 highest in *r*BCc among the three episodes (Figs. 15i-l and Figs. S12i-k), therefore it

https://doi.org/10.5194/acp-2022-194
Preprint. Discussion started: 6 April 2022


Atmospheric Chemistry and Physics Discussions

was also a period with influence from aged ship-emitted particles; the difference from EP2 is that photochemically formed sulfate and SOA were still significant as EP3 was in the later afternoon and early evening, though heterogeneously formed nitrate played a non-negligible role too (see the increase of RH, increase of nitrate and decrease of O_3 concentrations from the beginning of EP3 in Fig. 15).

4. Conclusions and implications

We conducted a field measurement during November of 2018 in urban Shanghai, China, focusing on the elucidation of physical and chemical properties of the ambient particles containing *r*BC cores (*r*BCc) by using a laser-only SP-AMS together with a HR-AMS. The campaign-average *r*BCc was 4.6 μg m^{-3}, occupying ~19.1% mass of the total NR-PM_1. The average mass ratio of coating to *r*BC cores (R_{BC}) was ~5.0, indicating an overall thick coating, compared with the *r*BCc near combustion source. Sulfate was found to preferentially condense on non-*r*BC particles thus led to a low fraction of *r*BCc sulfate to that in NR-PM_1 (7.4%), while distribution of nitrate between *r*BCc and non-rBC particles showed no obvious difference. PMF analysis on *r*BCc and NR-PM_1 OA reveals that cooking-related organics were externally mixed with *r*BC, and a small portion of organics from biomass burning was only present in *r*BCc; the traffic-related OA species, however, was in a large part internally mixed with *r*BC.

A regression algorithm was applied to deconvolute the size distributions of individual *r*BCc OA factors, and results show that small *r*BCc particles were predominantly generated from traffic, and such particles could grow bigger because of condensation of secondary inorganic and organic components, resulting in thick coating. Investigation on diurnal patterns of the *r*BCc species reveals that sulfate and two SOA factors (LO-OOA_{rBC} and MO-OOA_{rBC}) were generated mainly through daytime photochemical oxidation; nitrate, on the other hand, was governed mainly by the nocturnal N_2O_5 hydrolysis. Partial SOA was found to be produced from in-situ photochemical conversion from traffic-related POA. An average coating time (ACT) was proposed to roughly estimate the timescales for the secondary species to coat on *r*BC, and the ACT of sulfate, LO-OOA_{rBC}, MO-OOA_{rBC} and nitrate were approximately

https://doi.org/10.5194/acp-2022-194
Preprint. Discussion started: 6 April 2022


Atmospheric Chemistry and Physics Discussions

5, 5, 7 and 19 hours, respectively.

Moreover, the size-resolved hygroscopicity parameters of *r*BCc particles (κ_{rBCc}) and the coating material (κ_{CT}) were obtained based on the elucidated composition of *r*BCc particles. The fitted equations are: $\kappa_{rBCc}(x)= 0.29-0.14 \times \exp(-0.006 \times x)$ and $\kappa_{CT}(x) = 0.35 - 0.09 \times \exp(-0.003 \times x)$ (x is D_{rBCc}, $150<x<1000$ nm). The minimums of both κ_{rBCc} and κ_{CT} were at ~150 nm due to the abundances of hydrophobic *r*BC cores and traffic-related HOA at this size. Under critical supersaturations (SS_C) of 0.1% and 0.2%, the D_{50} values were estimated to be 166 ± 16 and 110 ± 5 nm, and the activated number fractions of *r*BCc particles were 16 ± 3% and 59 ± 4%, respectively. Finally, a typical case with influence from ship emissions was investigated. During this period, the *r*BCc particles were enriched in V (on average 5.8 ng m^{-3}), with a V/Ni ratio of 2.0, and various secondary formation processes affect the ship-emitted particles at different times of the day.

In summary, the findings from this comprehensive study on *r*BCc provide rich information regarding the various primary sources and secondary formation pathways of species coated on *r*BC, as well as the features of distributions of those species between *r*BC and non-rBC particles. In particular, different types of *r*BCc particles from diesel and gasoline vehicle emissions were resolved and elucidation of their properties are useful to their future effective control. Understanding of the formation processes and coating timescales of secondary components is helpful to understand the impact of ambient BC particles too. At last, the parameterized relationship of hygroscopicity with size distribution is useful for modelling the climate effect of *r*BC (alternation of cloud properties).

Data availability. The data in this study are available from the authors upon request (caxinra@163.com).

Supplement. The supplement related to this article is available online at: XXX

Author contributions. SJC, DDH, YZW, JFW, FZS, and XLG conducted the field

https://doi.org/10.5194/acp-2022-194
Preprint. Discussion started: 6 April 2022

measurement. SJC, DDH, YZW, JFW, and JKX analyzed the data. YJZ, HLW, CH and HL reviewed the paper and provide useful suggestions. SJC and XLG wrote the paper.

Competing interests. The contact author has declared that neither they nor their co-authors have any competing interests.

Disclaimer. Publisher's note: Copernicus Publications remains neutral with regard to jurisdictional claims in published maps and institutional affiliations.

Acknowledgements. We sincerely thank SAES to provide data of gaseous pollutants and particulate V and Ni, and the logistic help during the campaign.

Financial support. This work has been supported by the National Natural Science Foundation of China (42021004 and 21976093).

Review statement. This paper was XXX.

References

Aiken, A. C., DeCarlo, P. F., Kroll, J. H., Worsnop, D. R., Huffman, J. A., Docherty, K. S., Ulbrich, I. M., Mohr, C., Kimmel, J. R., Sueper, D., Sun, Y., Zhang, Q., Trimborn, A., Northway, M., Ziemann, P. J., Canagaratna, M. R., Onasch, T. B., Alfarra, M. R., Prevot, A. S. H., Dommen, J., Duplissy, J., Metzger, A., Baltensperger, U., and Jimenez, J. L.: O/C and OM/OC ratios of primary, secondary, and ambient organic aerosols with high-resolution time-of-flight aerosol mass spectrometry, Environ. Sci. Technol., 42, 4478-4485, https://doi.org/10.1021/es703009q, 2008.

Ault, A. P., Moore, M. J., Furutani, H., and Prather, K. A.: Impact of emissions from the Los Angeles port region on San Diego air quality during regional transport events, Environ. Sci. Technol., 43, 3500-3506, https://doi.org/10.1021/es8018918, 2009.

Ault, A. P., Gaston, C. I., Ying, W., Gerardo, D., Thiemens, M. H., and Prather, K.

https://doi.org/10.5194/acp-2022-194
Preprint. Discussion started: 6 April 2022


Atmospheric Chemistry and Physics Discussions

A.: Characterization of the single particle mixing state of individual ship plume events measured at the Port of Los Angeles, Environ. Sci. Technol., 44, 1954-1961, https://doi.org/10.1021/es902985h, 2010.

Becagli, S., Anello, F., Bommarito, C., Cassola, F., Calzolai, G., Di Iorio, T., di Sarra, A., Gómez-Amo, J.-L., Lucarelli, F., Marconi, M., Meloni, D., Monteleone, F., Nava, S., Pace, G., Severi, M., Sferlazzo, D. M., Traversi, R., and Udisti, R.: Constraining the ship contribution to the aerosol of the central Mediterranean, Atmos. Chem. Phys., 17, 2067-2084, https://doi.org/10.5194/acp-17-2067-2017, 2017.

Bond, T. C., Doherty, S. J., Fahey, D. W., Forster, P. M., Berntsen, T., DeAngelo, B. J., Flanner, M. G., Ghan, S., Kärcher, B., Koch, D., Kinne, S., Kondo, Y., Quinn, P. K., Sarofim, M. C., Schultz, M. G., Schulz, M., Venkataraman, C., Zhang, H., Zhang, S., Bellouin, N., Guttikunda, S. K., Hopke, P. K., Jacobson, M. Z., Kaiser, J. W., Klimont, Z., Lohmann, U., Schwarz, J. P., Shindell, D., Storelvmo, T., Warren, S. G., and Zender, C. S.: Bounding the role of black carbon in the climate system: A scientific assessment, J. Geophys. Res.: Atmos., 118, 5380-5552, https://doi.org/10.1002/jgrd.50171, 2013.

Canagaratna, M. R., Jayne, J. T., Jimenez, J. L., Allan, J. D., Alfarra, M. R., Zhang, Q., Onasch, T. B., Drewnick, F., Coe, H., Middlebrook, A., Delia, A., Williams, L. R., Trimborn, A. M., Northway, M. J., DeCarlo, P. F., Kolb, C. E., Davidovits, P., and Worsnop, D. R.: Chemical and microphysical characterization of ambient aerosols with the aerodyne aerosol mass spectrometer, Mass Spectrom. Rev., 26, 185-222, https://doi.org/10.1002/mas.20115, 2007.

Canagaratna, M. R., Jimenez, J. L., Kroll, J. H., Chen, Q., Kessler, S. H., Massoli, P., Hildebrandt Ruiz, L., Fortner, E., Williams, L. R., Wilson, K. R., Surratt, J. D., Donahue, N. M., Jayne, J. T., and Worsnop, D. R.: Elemental ratio measurements of organic compounds using aerosol mass spectrometry: characterization, improved calibration, and implications, Atmos. Chem. Phys., 15, 253-272, https://doi.org/10.5194/acp-15-253-2015, 2015a.

Canagaratna, M. R., Massoli, P., Browne, E. C., Franklin, J. P., Wilson, K. R., Onasch, T. B., Kirchstetter, T. W., Fortner, E. C., Kolb, C. E., Jayne, J. T., Kroll, J. H.,

https://doi.org/10.5194/acp-2022-194
Preprint. Discussion started: 6 April 2022


Atmospheric Chemistry and Physics Discussions

and Worsnop, D. R.: Chemical compositions of black carbon particle cores and coatings via soot particle aerosol mass spectrometry with photoionization and electron ionization, J. Phys. Chem. A, 119, 4589-4599, https://doi.org/10.1021/jp510711u, 2015b.

Cao, L.-M., Wei, J., He, L.-Y., Zeng, H., Li, M.-L., Zhu, Q., Yu, G.-H., and Huang, X.-F.: Aqueous aging of secondary organic aerosol coating onto black carbon: Insights from simultaneous L-ToF-AMS and SP-AMS measurements at an urban site in southern China, J. Clean Prod., 330, 129888, https://doi.org/10.1016/j.jclepro.2021.129888, 2022.

Cappa, C. D., Onasch, T. B., Massoli, P., Worsnop, D. R., Bates, T. S., Cross, E. S., Davidovits, P., Hakala, J., Hayden, K. L., Jobson, B. T., Kolesar, K. R., Lack, D. A., Lerner, B. M., Li, S.-M., Mellon, D., Nuaaman, I., Olfert, J. S., Petäjä, T., Quinn, P. K., Song, C., Subramanian, R., Williams, E. J., and Zaveri, R. A.: Radiative Absorption Enhancements Due to the Mixing State of Atmospheric Black Carbon, Science, 337, 1078-1081, https://doi.org/10.1126/science.1230260, 2012.

Chang, R. Y. W., Slowik, J. G., Shantz, N. C., Vlasenko, A., Liggio, J., Sjostedt, S. J., Leaitch, W. R., and Abbatt, J. P. D.: The hygroscopicity parameter (κ) of ambient organic aerosol at a field site subject to biogenic and anthropogenic influences: relationship to degree of aerosol oxidation, Atmos. Chem. Phys., 10, 5047-5064, https://doi.org/10.5194/acp-10-5047-2010, 2010.

Chen, B., Bai, Z., Cui, X., Chen, J., Andersson, A., and Gustafsson, O.: Light absorption enhancement of black carbon from urban haze in Northern China winter, Environ. Pollut., 221, 418-426, https://doi.org/10.1016/j.envpol.2016.12.004, 2017.

Chen, C., Fan, X., Shaltout, T., Qiu, C., Ma, Y., Goldman, A., and Khalizov, A. F.: An unexpected restructuring of combustion soot aggregates by subnanometer coatings of polycyclic aromatic hydrocarbons, Geophys. Res. Lett., 43, 11,080-011,088, https://doi.org/10.1002/2016GL070877, 2016.

Chen, C., Enekwizu, O. Y., Fan, X., Dobrzanski, C. D., Ivanova, E. V., Ma, Y., Gor, G. Y., and Khalizov, A. F.: Single Parameter for Predicting the Morphology of Atmospheric Black Carbon, Environ. Sci. Technol., 52, 14169-14179, https://doi.org/10.1021/acs.est.8b04201, 2018.

https://doi.org/10.5194/acp-2022-194
Preprint. Discussion started: 6 April 2022


Atmospheric Chemistry and Physics Discussions

Chen, D., Tian, X., Lang, J., Zhou, Y., Li, Y., Guo, X., Wang, W., and Liu, B.: The impact of ship emissions on $PM_{2.5}$ and the deposition of nitrogen and sulfur in Yangtze River Delta, China, Sci. Total Environ., 649, 1609-1619, https://doi.org/10.1016/j.scitotenv.2018.08.313, 2019.

Clegg, S. L., Brimblecombe, P., and Wexler, A. S.: Thermodynamic model of the system H^+ NH_4^+ – SO_4^{2-} – NO_3^- – H_2O at tropospheric temperatures, 102, 2155–2171, https://doi.org/10.1021/jp973043j, 1998.

Collier, S., Williams, L. R., Onasch, T. B., Cappa, C. D., Zhang, X., Russell, L. M., Chen, C.-L., Sanchez, K. J., Worsnop, D. R., and Zhang, Q.: Influence of Emissions and Aqueous Processing on Particles Containing Black Carbon in a Polluted Urban Environment: Insights From a Soot Particle-Aerosol Mass Spectrometer, J. Geophys. Res.: Atmos., 123, 6648-6666, https://doi.org/10.1002/2017jd027851, 2018.

Corbin, J. C., Sierau, B., Gysel, M., Laborde, M., Keller, A., Kim, J., Petzold, A., Onasch, T. B., Lohmann, U., and Mensah, A. A.: Mass spectrometry of refractory black carbon particles from six sources: carbon-cluster and oxygenated ions, Atmos. Chem. Phys., 14, 2591-2603, https://doi.org/10.5194/acp-14-2591-2014, 2014.

Cubison, M. J., Ortega, A. M., Hayes, P. L., Farmer, D. K., Day, D., Lechner, M. J., Brune, W. H., Apel, E., Diskin, G. S., Fisher, J. A., Fuelberg, H. E., Hecobian, A., Knapp, D. J., Mikoviny, T., Riemer, D., Sachse, G. W., Sessions, W., Weber, R. J., Weinheimer, A. J., Wisthaler, A., and Jimenez, J. L.: Effects of aging on organic aerosol from open biomass burning smoke in aircraft and laboratory studies, Atmos. Chem. Phys., 11, 12049-12064, https://doi.org/10.5194/acp-11-12049-2011, 2011.

DeCarlo, P. F., Kimmel, J. R., Trimborn, A., Northway, M. J., Jayne, J. T., Aiken, A. C., Gonin, M., Fuhrer, K., Horvath, T., Docherty, K. S., Worsnop, D. R., and Jimenez, J. L.: Field-Deployable, High-Resolution, Time-of-Flight Aerosol Mass Spectrometer, Anal. Chem. , 78, 8281-8289, https://doi.org/10.1021/ac061249n, 2006.

Enroth, J., Saarikoski, S., Niemi, J., Kousa, A., Ježek, I., Močnik, G., Carbone, S., Kuuluvainen, H., Rönkkö, T., Hillamo, R., and Pirjola, L.: Chemical and physical characterization of traffic particles in four different highway environments in the

https://doi.org/10.5194/acp-2022-194
Preprint. Discussion started: 6 April 2022


Atmospheric Chemistry and Physics Discussions

949 Helsinki metropolitan area, Atmos. Chem. Phys., 16, 5497-5512,
950 https://doi.org/10.5194/acp-16-5497-2016, 2016.
951 Fan, Q., Zhang, Y., Ma, W., Ma, H., Feng, J., Yu, Q., Yang, X., Ng, S. K., Fu, Q.,
952 and Chen, L.: Spatial and Seasonal Dynamics of Ship Emissions over the Yangtze River
953 Delta and East China Sea and Their Potential Environmental Influence, Environ. Sci.
954 Technol., 50, 1322-1329, https://doi.org/10.1021/acs.est.5b03965, 2016.
955 Gao, X., Yang, L., Cheng, S., Gao, R., Zhou, Y., Xue, L., Shou, Y., Wang, J., Wang,
956 X., Nie, W., Xu, P., and Wang, W.: Semi-continuous measurement of water-soluble ions
957 in $PM_{2.5}$ in Jinan, China: Temporal variations and source apportionments, Atmos.
958 Environ., 45, 6048-6056, https://doi.org/10.1016/j.atmosenv.2011.07.041, 2011.
959 Ge, X., Zhang, Q., Sun, Y., Ruehl, C. R., and Setyan, A.: Effect of aqueous-phase
960 processing on aerosol chemistry and size distributions in Fresno, California, during
961 wintertime, Environ. Chem., 9, 221-235, https://doi.org/10.1071/EN11168, 2012.
962 Gilardoni, S., Massoli, P., Paglione, M., Giulianelli, L., Carbone, C., Rinaldi, M.,
963 Decesari, S., Sandrini, S., Costabile, F., Gobbi, G. P., Pietrogrande, M. C., Visentin, M.,
964 Scotto, F., Fuzzi, S., and Facchini, M. C.: Direct observation of aqueous secondary
965 organic aerosol from biomass-burning emissions, Proc. Natl. Acad. Sci. U. S. A., 113,
966 10013-10018, https://doi.org/10.1073/pnas.1602212113, 2016.
967 Gong, X., Zhang, C., Chen, H., Nizkorodov, S. A., Chen, J., and Yang, X.: Size
968 distribution and mixing state of black carbon particles during a heavy air pollution
969 episode in Shanghai, Atmos. Chem. Phys., 16, 5399-5411, https://doi.org/10.5194/acp-
970 16-5399-2016, 2016.
971 Gysel, M., Crosier, J., Topping, D. O., Whitehead, J. D., Bower, K. N., Cubison,
972 M. J., Williams, P. I., Flynn, M. J., McFiggans, G. B., and Coe, H.: Closure study
973 between chemical composition and hygroscopic growth of aerosol particles during
974 TORCH2, Atmos. Chem. Phys., 7, 6131-6144, https://doi.org/10.5194/acp-7-6131-
975 2007, 2007.
976 Heald, C. L., Kroll, J. H., Jimenez, J. L., Docherty, K. S., DeCarlo, P. F., Aiken, A.
977 C., Chen, Q., Martin, S. T., Farmer, D. K., and Artaxo, P.: A simplified description of
978 the evolution of organic aerosol composition in the atmosphere, Geophys. Res. Lett.,

https://doi.org/10.5194/acp-2022-194
Preprint. Discussion started: 6 April 2022


Atmospheric Chemistry and Physics Discussions

37, https://doi.org/10.1029/2010gl042737, 2010.

Hu, D., Liu, D., Kong, S., Zhao, D., Wu, Y., Li, S., Ding, S., Zheng, S., Cheng, Y., Hu, K., Deng, Z., Wu, Y., Tian, P., Liu, Q., Huang, M., and Ding, D.: Direct Quantification of Droplet Activation of Ambient Black Carbon Under Water Supersaturation, J. Geophys. Res.: Atmos., 126, e2021JD034649, https://doi.org/10.1029/2021jd034649, 2021.

Jacobi, H. W., Lim, S., Ménégoz, M., Ginot, P., Laj, P., Bonasoni, P., Stocchi, P., Marinoni, A., and Arnaud, Y.: Black carbon in snow in the upper Himalayan Khumbu Valley, Nepal: observations and modeling of the impact on snow albedo, melting, and radiative forcing, The Cryosphere, 9, 1685-1699, https://doi.org/10.5194/tc-9-1685-2015, 2015.

Jang, H.-N., Seo, Y.-C., Lee, J.-H., Hwang, K.-W., Yoo, J.-I., Sok, C.-H., and Kim, S.-H.: Formation of fine particles enriched by V and Ni from heavy oil combustion: anthropogenic sources and drop-tube furnace experiments, Atmos. Environ., 41, 1053-1063, https://doi.org/10.1016/j.atmosenv.2006.09.011, 2007.

Jayne, J. T., Leard, D. C., Zhang, X., Davidovits, P., Smith, K. A., Kolb, C. E., and Worsnop, D. R.: Development of an aerosol mass spectrometer for size and composition analysis of submicron particles, Aerosol Sci. Technol., 33, 49-70, https://doi.org/10.1080/027868200410840, 2000.

Kim, K.-H., Shon, Z.-H., Mauulida, P. T., and Song, S.-K.: Long-term monitoring of airborne nickel (Ni) pollution in association with some potential source processes in the urban environment, Chemosphere, 111, 312-319, https://doi.org/10.1016/j.chemosphere.2014.03.138, 2014.

Kroll, J. H., Donahue, N. M., Jimenez, J. L., Kessler, S. H., Canagaratna, M. R., Wilson, K. R., Altieri, K. E., Mazzoleni, L. R., Wozniak, A. S., Bluhm, H., Mysak, E. R., Smith, J. D., Kolb, C. E., and Worsnop, D. R.: Carbon oxidation state as a metric for describing the chemistry of atmospheric organic aerosol, Nat. Chem., 3, 133-139, https://doi.org/10.1038/nchem.948, 2011.

Lambe, A. T., Ahern, A. T., Wright, J. P., Croasdale, D. R., Davidovits, P., and Onasch, T. B.: Oxidative aging and cloud condensation nuclei activation of laboratory

https://doi.org/10.5194/acp-2022-194
Preprint. Discussion started: 6 April 2022


Atmospheric Chemistry and Physics Discussions

1009 combustion soot, J. Aerosol. Sci., 79, 31-39,
1010 https://doi.org/10.1016/j.jaerosci.2014.10.001, 2015.
1011 Laskin, A., Smith, J. S., and Laskin, J.: Molecular characterization of nitrogen-
1012 containing organic compounds in biomass burning aerosols using high-resolution mass
1013 spectrometry, Environ. Sci. Technol., 43, 3764-3771,
1014 https://doi.org/10.1021/es803456n, 2009.
1015 Lee, A. K. Y., Willis, M. D., Healy, R. M., Onasch, T. B., and Abbatt, J. P. D.:
1016 Mixing state of carbonaceous aerosol in an urban environment: single particle
1017 characterization using the soot particle aerosol mass spectrometer (SP-AMS), Atmos.
1018 Chem. Phys., 15, 1823-1841, https://doi.org/10.5194/acp-15-1823-2015, 2015.
1019 Lee, A. K. Y., Chen, C.-L., Liu, J., Price, D. J., Betha, R., Russell, L. M., Zhang,
1020 X., and Cappa, C. D.: Formation of secondary organic aerosol coating on black carbon
1021 particles near vehicular emissions, Atmos. Chem. Phys., 17, 15055-15067,
1022 https://doi.org/10.5194/acp-17-15055-2017, 2017.
1023 Lee, A. K. Y., Rivellini, L. H., Chen, C. L., Liu, J., Price, D. J., Betha, R., Russell,
1024 L. M., Zhang, X., and Cappa, C. D.: Influences of primary emission and secondary
1025 coating formation on the particle diversity and mixing state of black carbon particles,
1026 Environ. Sci. Technol., 53, 9429-9438, https://doi.org/10.1021/acs.est.9b03064, 2019.
1027 Li, W., Teng, X., Chen, X., Liu, L., Xu, L., Zhang, J., Wang, Y., Zhang, Y., and Shi,
1028 Z.: Organic coating reduces hygroscopic growth of phase-separated aerosol particles,
1029 Environ. Sci. Technol., 55, 16339–16346, https://doi.org/10.1021/acs.est.1c05901,
1030 2021.
1031 Liu, D., Allan, J., Whitehead, J., Young, D., Flynn, M., Coe, H., McFiggans, G.,
1032 Fleming, Z. L., and Bandy, B.: Ambient black carbon particle hygroscopic properties
1033 controlled by mixing state and composition, Atmos. Chem. Phys., 13, 2015-2029,
1034 https://doi.org/10.5194/acp-13-2015-2013, 2013.
1035 Liu, D., Whitehead, J., Alfarra, M. R., Reyes-Villegas, E., Spracklen, Dominick V.,
1036 Reddington, Carly L., Kong, S., Williams, Paul I., Ting, Y.-C., Haslett, S., Taylor,
1037 Jonathan W., Flynn, Michael J., Morgan, William T., McFiggans, G., Coe, H., and
1038 Allan, James D.: Black-carbon absorption enhancement in the atmosphere determined

https://doi.org/10.5194/acp-2022-194
Preprint. Discussion started: 6 April 2022


Atmospheric Chemistry and Physics Discussions

1039 by particle mixing state, Nat. Geosci., 10, 184-188, https://doi.org/10.1038/ngeo2901,
1040 2017a.
1041 Liu, D., Joshi, R., Wang, J., Yu, C., Allan, J. D., Coe, H., Flynn, M. J., Xie, C., Lee,
1042 J., Squires, F., Kotthaus, S., Grimmond, S., Ge, X., Sun, Y., and Fu, P.: Contrasting
1043 physical properties of black carbon in urban Beijing between winter and summer,
1044 Atmos. Chem. Phys., 19, 6749-6769, https://doi.org/10.5194/acp-19-6749-2019, 2019.
1045 Liu, S., Aiken, A. C., Gorkowski, K., Dubey, M. K., Cappa, C. D., Williams, L. R.,
1046 Herndon, S. C., Massoli, P., Fortner, E. C., Chhabra, P. S., Brooks, W. A., Onasch, T.
1047 B., Jayne, J. T., Worsnop, D. R., China, S., Sharma, N., Mazzoleni, C., Xu, L., Ng, N.
1048 L., Liu, D., Allan, J. D., Lee, J. D., Fleming, Z. L., Mohr, C., Zotter, P., Szidat, S., and
1049 Prevot, A. S. H.: Enhanced light absorption by mixed source black and brown carbon
1050 particles in UK winter, Nat. Commun., 6, 8435, https://doi.org/10.1038/ncomms9435,
1051 2015.
1052 Liu, Z., Lu, X., Feng, J., Fan, Q., Zhang, Y., and Yang, X.: Influence of ship
1053 emissions on urban air quality: a Comprehensive study using highly time-resolved
1054 online measurements and numerical simulation in Shanghai, Environ. Sci. Technol., 51,
1055 202-211, https://doi.org/10.1021/acs.est.6b03834, 2017b.
1056 Malmborg, V. B., Eriksson, A. C., Shen, M., Nilsson, P., Gallo, Y., Waldheim, B.,
1057 Martinsson, J., Andersson, O., and Pagels, J.: Evolution of In-Cylinder Diesel Engine
1058 Soot and Emission Characteristics Investigated with Online Aerosol Mass Spectrometry,
1059 Environ. Sci. Technol., 51, 1876-1885, https://doi.org/10.1021/acs.est.6b03391, 2017.
1060 Mar, V., Fulvio, A., Andrés, A., Xavier, Q., Teresa, M., Saúl García, D. S., María
1061 Dolores, H., and Rosalía, F. P.: Chemical tracers of particulate emissions from
1062 commercial shipping, Environ. Sci. Technol., 43, 7472-7477,
1063 https://doi.org/10.1021/es901558t, 2009.
1064 Massoli, P., Fortner, E. C., Canagaratna, M. R., Williams, L. R., Zhang, Q., Sun,
1065 Y., Schwab, J. J., Trimborn, A., Onasch, T. B., Demerjian, K. L., Kolb, C. E., Worsnop,
1066 D. R., and Jayne, J. T.: Pollution Gradients and Chemical Characterization
1067 of Particulate Matter from Vehicular Traffic near Major Roadways: Results from the
1068 2009 Queens College Air Quality Study in NYC, Aerosol Sci. Technol., 46, 1201-1218,

https://doi.org/10.5194/acp-2022-194
Preprint. Discussion started: 6 April 2022


Atmospheric Chemistry and Physics Discussions

https://doi.org/10.1080/02786826.2012.701784, 2012.

Massoli, P., Onasch, T. B., Cappa, C. D., Nuamaan, I., Hakala, J., Hayden, K., Li, S.-M., Sueper, D. T., Bates, T. S., Quinn, P. K., Jayne, J. T., and Worsnop, D. R.: Characterization of black carbon-containing particles from soot particle aerosol mass spectrometer measurements on the R/VAtlantisduring CalNex 2010, J. Geophys. Res.: Atmos., 120, 2575-2593, https://doi.org/10.1002/2014jd022834, 2015.

Mazzei, F., D'Alessandro, A., Lucarelli, F., Nava, S., Prati, P., Valli, G., and Vecchi, R.: Characterization of particulate matter sources in an urban environment, Sci. Total Environ., 401, 81-89, https://doi.org/10.1016/j.scitotenv.2008.03.008, 2008.

Mohr, C., Huffman, J. A., Cubison, M. J., Aiken, A. C., Docherty, K. S., Kimmel, J. R., Ulbrich, I. M., Hannigan, M., and Jimenez, J. L.: Characterization of Primary Organic Aerosol Emissions from Meat Cooking, Trash Burning, and Motor Vehicles with High-Resolution Aerosol Mass Spectrometry and Comparison with Ambient and Chamber Observations, Environ. Sci. Technol., 43, 2443-2449, https://doi.org/10.1021/es8011518, 2009.

Moldanová, J., Fridell, E., Popovicheva, O., Demirdjian, B., Tishkova, V., Faccinetto, A., and Focsa, C.: Characterisation of particulate matter and gaseous emissions from a large ship diesel engine, Atmos. Environ., 43, 2632-2641, https://doi.org/10.1016/j.atmosenv.2009.02.008, 2009.

Ng, N. L., Canagaratna, M. R., Jimenez, J. L., Chhabra, P. S., Seinfeld, J. H., and Worsnop, D. R.: Changes in organic aerosol composition with aging inferred from aerosol mass spectra, Atmos. Chem. Phys., 11, 6465-6474, https://doi.org/10.5194/acp-11-6465-2011, 2011.

Onasch, T. B., Trimborn, A., Fortner, E. C., Jayne, J. T., Kok, G. L., Williams, L. R., Davidovits, P., and Worsnop, D. R.: Soot Particle Aerosol Mass Spectrometer: Development, Validation, and Initial Application, Aerosol Sci. Technol., 46, 804-817, https://doi.org/10.1080/02786826.2012.663948, 2012.

Paatero, P., and Tapper, U.: Positive matrix factorization: A non-negative factor model with optimal utilization of error estimates of data values, Environmetrics, 5, 111-126, https://doi.org/10.1002/env.3170050203, 1994.

https://doi.org/10.5194/acp-2022-194
Preprint. Discussion started: 6 April 2022


Atmospheric Chemistry and Physics Discussions

1099 Pathak, R. K., Wang, T., and Wu, W. S.: Nighttime enhancement of $PM_{2.5}$ nitrate
1100 in ammonia-poor atmospheric conditions in Beijing and Shanghai: Plausible
1101 contributions of heterogeneous hydrolysis of N_2O_5 and HNO_3 partitioning, Atmos.
1102 Environ., 45, 1183-1191, https://doi.org/10.1016/j.atmosenv.2010.09.003, 2011.
1103 Peng, J., Hu, M., Guo, S., Du, Z., Zheng, J., Shang, D., Levy, Z. M., Zeng, L.,
1104 Shao, M., and Wu, Y. S.: Markedly enhanced absorption and direct radiative forcing of
1105 black carbon under polluted urban environments, Proc. Natl. Acad. Sci. U. S. A., 113,
1106 4266-4271, https://doi.org/10.1073/pnas.1602310113, 2016.
1107 Petit, J. E., Favez, O., Albinet, A., and Canonaco, F.: A user-friendly tool for
1108 comprehensive evaluation of the geographical origins of atmospheric pollution: Wind
1109 and trajectory analyses, 88, 183-187, https://doi.org/10.1016/j.envsoft.2016.11.022,
1110 2017.
1111 Petters, M. D., and Kreidenweis, S. M.: A single parameter representation of
1112 hygroscopic growth and cloud condensation nucleus activity, Atmos. Chem. Phys., 7,
1113 1961-1971, https://doi.org/10.5194/acp-7-1961-2007, 2007.
1114 Ramanathan, V., and Carmichael, G.: Global and regional climate changes due to
1115 black carbon, Nat. Geosci., 1, 221-227, https://doi.org/10.1038/ngeo156, 2008.
1116 Rivellini, L.-H., Adam, M. G., Kasthuriarachchi, N., and Lee, A. K. Y.:
1117 Characterization of carbonaceous aerosols in Singapore: insight from black carbon
1118 fragments and trace metal ions detected by a soot particle aerosol mass spectrometer,
1119 Atmos. Chem. Phys., 20, 5977-5993, https://doi.org/10.5194/acp-20-5977-2020, 2020.
1120 Saarikoski, S., Timonen, H., Carbone, S., Kuuluvainen, H., Niemi, J. V., Kousa,
1121 A., Rönkkö, T., Worsnop, D., Hillamo, R., and Pirjola, L.: Investigating the chemical
1122 species in submicron particles emitted by city buses, Aerosol Sci. Technol., 51, 317-
1123 329, https://doi.org/10.1080/02786826.2016.1261992, 2016.
1124 Sun, Y. L., Zhang, Q., Schwab, J. J., Demerjian, K. L., Chen, W. N., Bae, M. S.,
1125 Hung, H. M., Hogrefe, O., Frank, B., Rattigan, O. V., and Lin, Y. C.: Characterization
1126 of the sources and processes of organic and inorganic aerosols in New York city with a
1127 high-resolution time-of-flight aerosol mass apectrometer, Atmos. Chem. Phys., 11,
1128 1581-1602, https://doi.org/10.5194/acp-11-1581-2011, 2011.

https://doi.org/10.5194/acp-2022-194
Preprint. Discussion started: 6 April 2022

1129 Sun, Y. L., Zhang, Q., Schwab, J. J., Yang, T., Ng, N. L., and Demerjian, K. L.:
1130 Factor analysis of combined organic and inorganic aerosol mass spectra from high
1131 resolution aerosol mass spectrometer measurements, Atmos. Chem. Phys., 12, 8537-
1132 8551, https://doi.org/10.5194/acp-12-8537-2012, 2012.
1133 Topping, D. O., McFiggans, G. B., and Coe, H.: A curved multi-component aerosol
1134 hygroscopicity model framework: Part 1 – Inorganic compounds, Atmos. Chem. Phys.,
1135 5, 1205-1222, https://doi.org/10.5194/acp-5-1205-2005, 2005a.
1136 Topping, D. O., McFiggans, G. B., and Coe, H.: A curved multi-component aerosol
1137 hygroscopicity model framework: Part 2 – Including organic compounds, Atmos. Chem.
1138 Phys., 5, 1223-1242, https://doi.org/10.5194/acp-5-1223-2005, 2005b.
1139 Ulbrich, I. M., Canagaratna, M. R., Zhang, Q., Worsnop, D. R., and Jimenez, J. L.:
1140 Interpretation of organic components from Positive Matrix Factorization of aerosol
1141 mass spectrometric data, Atmos. Chem. Phys., 9, 2891-2918,
1142 https://doi.org/10.5194/acp-9-2891-2009, 2009.
1143 Ulbrich, I. M., Canagaratna, M. R., Cubison, M. J., Zhang, Q., Ng, N. L., Aiken,
1144 A. C., and Jimenez, J. L.: Three-dimensional factorization of size-resolved organic
1145 aerosol mass spectra from Mexico City, Atmos. Meas. Tech., 5, 195-224,
1146 https://doi.org/10.5194/amt-5-195-2012, 2012.
1147 Wang, J., Ge, X., Chen, Y., Shen, Y., Zhang, Q., Sun, Y., Xu, J., Ge, S., Yu, H., and
1148 Chen, M.: Highly time-resolved urban aerosol characteristics during springtime in
1149 Yangtze River Delta, China: insights from soot particle aerosol mass spectrometry,
1150 Atmos. Chem. Phys., 16, 9109-9127, https://doi.org/10.5194/acp-16-9109-2016, 2016.
1151 Wang, J., Zhang, Q., Chen, M., Collier, S., Zhou, S., Ge, X., Xu, J., Shi, J., Xie,
1152 C., Hu, J., Ge, S., Sun, Y., and Coe, H.: First Chemical Characterization of Refractory
1153 Black Carbon Aerosols and Associated Coatings over the Tibetan Plateau (4730 m a.s.l),
1154 Environ. Sci. Technol., 51, 14072-14082, https://doi.org/10.1021/acs.est.7b03973,
1155 2017.
1156 Wang, J., Liu, D., Ge, X., Wu, Y., Shen, F., Chen, M., Zhao, J., Xie, C., Wang, Q.,
1157 Xu, W., Zhang, J., Hu, J., Allan, J., Joshi, R., Fu, P., Coe, H., and Sun, Y.:
1158 Characterization of black carbon-containing fine particles in Beijing during wintertime,

https://doi.org/10.5194/acp-2022-194
Preprint. Discussion started: 6 April 2022


Atmospheric Chemistry and Physics Discussions

1159 Atmos. Chem. Phys., 19, 447-458, https://doi.org/10.5194/acp-19-447-2019, 2019.
1160 Wang, J., Ye, J., Liu, D., Wu, Y., Zhao, J., Xu, W., Xie, C., Shen, F., Zhang, J.,
1161 Ohno, P. E., Qin, Y., Zhao, X., Martin, S. T., Lee, A. K. Y., Fu, P., Jacob, D. J., Zhang,
1162 Q., Sun, Y., Chen, M., and Ge, X.: Characterization of submicron organic particles in
1163 Beijing during summertime: comparison between SP-AMS and HR-AMS, Atmos.
1164 Chem. Phys., 20, 14091-14102, https://doi.org/10.5194/acp-20-14091-2020, 2020a.
1165 Wang, J., Ye, J., Zhang, Q., Zhao, J., Wu, Y., Li, J., Liu, D., Li, W., Zhang, Y., Wu,
1166 C., Xie, C., Qin, Y., Lei, Y., Huang, X., Guo, J., Liu, P., Fu, P., Li, Y., Lee, H. C., Choi,
1167 H., Zhang, J., Liao, H., Chen, M., Sun, Y., Ge, X., Martin, S. T., and Jacob, D. J.:
1168 Aqueous production of secondary organic aerosol from fossil-fuel emissions in winter
1169 Beijing haze, Proc. Natl. Acad. Sci. U. S. A., 118, e2022179118,
1170 https://doi.org/10.1073/pnas.2022179118, 2021.
1171 Wang, S., Newland, M. J., Deng, W., Rickard, A. R., Hamilton, J. F., Muñoz, A.,
1172 Ródenas, M., Vázquez, M. M., Wang, L., and Wang, X.: Aromatic Photo-oxidation, A
1173 New Source of Atmospheric Acidity, Environ. Sci. Technol., 54, 7798-7806,
1174 https://doi.org/10.1021/acs.est.0c00526, 2020b.
1175 Willis, M. D., Healy, R. M., Riemer, N., West, M., Wang, J. M., Jeong, C.-H.,
1176 Wenger, J. C., Evans, G. J., Abbatt, J. P. D., and Lee, A. K. Y.: Quantification of black
1177 carbon mixing state from traffic: implications for aerosol optical properties, Atmos.
1178 Chem. Phys., 16, 4693-4706, https://doi.org/10.5194/acp-16-4693-2016, 2016.
1179 Wu, Y., Ge, X., Wang, J., Shen, Y., Ye, Z., Ge, S., Wu, Y., Yu, H., and Chen, M.:
1180 Responses of secondary aerosols to relative humidity and photochemical activities in
1181 an industrialized environment during late winter, Atmos. Environ., 193, 66-78,
1182 https://doi.org/10.1016/j.atmosenv.2018.09.008, 2018.
1183 Wu, Y., Liu, D., Wang, J., Shen, F., Chen, Y., Cui, S., Ge, S., Wu, Y., Chen, M.,
1184 and Ge, X.: Characterization of Size-Resolved Hygroscopicity of Black Carbon-
1185 Containing Particle in Urban Environment, Environ. Sci. Technol., 53, 14212-14221,
1186 https://doi.org/10.1021/acs.est.9b05546, 2019.
1187 Wu, Y., Liu, D., Wang, X., Li, S., Zhang, J., Qiu, H., Ding, S., Hu, K., Li, W., Tian,
1188 P., Liu, Q., Zhao, D., Ma, E., Chen, M., Xu, H., Ouyang, B., Chen, Y., Kong, S., Ge, X.,

https://doi.org/10.5194/acp-2022-194
Preprint. Discussion started: 6 April 2022


Atmospheric Chemistry and Physics Discussions

1189 and Liu, H.: Ambient marine shipping emissions determined by vessel operation mode
1190 along the East China Sea, Sci. Total Environ., 769, 144713,
1191 https://doi.org/10.1016/j.scitotenv.2020.144713, 2021.
1192 Wu, Z. J., Zheng, J., Shang, D. J., Du, Z. F., Wu, Y. S., Zeng, L. M., Wiedensohler,
1193 A., and Hu, M.: Particle hygroscopicity and its link to chemical composition in the
1194 urban atmosphere of Beijing, China, during summertime, Atmos. Chem. Phys., 16,
1195 1123-1138, https://doi.org/10.5194/acp-16-1123-2016, 2016.
1196 Xie, C., Xu, W., Wang, J., Liu, D., Ge, X., Zhang, Q., Wang, Q., Du, W., Zhao, J.,
1197 Zhou, W., Li, J., Fu, P., Wang, Z., Worsnop, D., and Sun, Y.: Light absorption
1198 enhancement of black carbon in urban Beijing in summer, Atmos. Environ., 213, 499-
1199 504, https://doi.org/10.1016/j.atmosenv.2019.06.041, 2019.
1200 Xu, J., Zhang, Q., Chen, M., Ge, X., Ren, J., and Qin, D.: Chemical composition,
1201 sources, and processes of urban aerosols during summertime in northwest China:
1202 insights from high-resolution aerosol mass spectrometry, Atmos. Chem. Phys., 14,
1203 12593-12611, https://doi.org/10.5194/acp-14-12593-2014, 2014.
1204 Xu, W., Han, T., Du, W., Wang, Q., Chen, C., Zhao, J., Zhang, Y., Li, J., Fu, P.,
1205 Wang, Z., Worsnop, D. R., and Sun, Y.: Effects of Aqueous-Phase and Photochemical
1206 Processing on Secondary Organic Aerosol Formation and Evolution in Beijing, China,
1207 Environ. Sci. Technol., 51, 762-770, https://doi.org/10.1021/acs.est.6b04498, 2017.
1208 Xu, W., Sun, Y., Wang, Q., Zhao, J., Wang, J., Ge, X., Xie, C., Zhou, W., Du, W.,
1209 Li, J., Fu, P., Wang, Z., Worsnop, D. R., and Coe, H.: Changes in Aerosol Chemistry
1210 From 2014 to 2016 in Winter in Beijing: Insights From High-Resolution Aerosol Mass
1211 Spectrometry, J. Geophys. Res.: Atmos., 124, 1132-1147,
1212 https://doi.org/10.1029/2018jd029245, 2019.
1213 Ye, Z., Liu, J., Gu, A., Feng, F., Liu, Y., Bi, C., Xu, J., Li, L., Chen, H., Chen, Y.,
1214 Dai, L., Zhou, Q., and Ge, X.: Chemical characterization of fine particulate matter in
1215 Changzhou, China, and source apportionment with offline aerosol mass spectrometry,
1216 Atmos. Chem. Phys., 17, 2573-2592, https://doi.org/10.5194/acp-17-2573-2017, 2017.
1217 Yu, G., Zhang, Y., Yang, F., He, B., Zhang, C., Zou, Z., Yang, X., Li, N., and Chen,
1218 J.: Dynamic Ni/V Ratio in the Ship-Emitted Particles Driven by Multiphase Fuel Oil

https://doi.org/10.5194/acp-2022-194
Preprint. Discussion started: 6 April 2022


Atmospheric Chemistry and Physics Discussions

1219 Regulations in Coastal China, Environ. Sci. Technol., 55, 15031-15039,
1220 https://doi.org/10.1021/acs.est.1c02612, 2021.
1221 Yu, L., Smith, J., Laskin, A., Anastasio, C., Laskin, J., and Zhang, Q.: Chemical
1222 characterization of SOA formed from aqueous-phase reactions of phenols with the
1223 triplet excited state of carbonyl and hydroxyl radical, Atmos. Chem. Phys., 14, 13801-
1224 13816, https://doi.org/10.5194/acp-14-13801-2014, 2014.
1225 Zhang, F., Wang, Y., Peng, J., Chen, L., Sun, Y., Duan, L., Ge, X., Li, Y., Zhao, J.,
1226 Liu, C., Zhang, X., Zhang, G., Pan, Y., Wang, Y., Zhang Annie, L., Ji, Y., Wang, G., Hu,
1227 M., Molina Mario, J., and Zhang, R.: An unexpected catalyst dominates formation and
1228 radiative forcing of regional haze, Proc. Natl. Acad. Sci. U. S. A., 117, 3960-3966,
1229 https://doi.org/10.1073/pnas.1919343117, 2020.
1230 Zhang, G., Fu, Y., Peng, X., Sun, W., Shi, Z., Song, W., Hu, W., Chen, D., Lian,
1231 X., Li, L., Tang, M., Wang, X., and Bi, X.: Black Carbon Involved Photochemistry
1232 Enhances the Formation of Sulfate in the Ambient Atmosphere: Evidence From In Situ
1233 Individual Particle Investigation, J. Geophys. Res.: Atmos., 126, e2021JD035226,
1234 https://doi.org/10.1029/2021JD035226, 2021.
1235 Zhang, Q., Canagaratna, M. R., Jayne, J. T., Worsnop, D. R., and Jimenez, J.-L.:
1236 Time- and size-resolved chemical composition of submicron particles in Pittsburgh:
1237 Implications for aerosol sources and processes, J. Geophys. Res., 110,
1238 https://doi.org/10.1029/2004JD004649, 2005.
1239 Zhang, Q., Jimenez, J. L., Canagaratna, M. R., Ulbrich, I. M., Ng, N. L., Worsnop,
1240 D. R., and Sun, Y.: Understanding atmospheric organic aerosols via factor analysis of
1241 aerosol mass spectrometry: a review, Anal. Bioanal. Chem., 401, 3045-3067,
1242 https://doi.org/10.1007/s00216-011-5355-y, 2011.
1243 Zhao, J., Qiu, Y., Zhou, W., Xu, W., Wang, J., Zhang, Y., Li, L., Xie, C., Wang, Q.,
1244 Du, W., Worsnop, D. R., Canagaratna, M. R., Zhou, L., Ge, X., Fu, P., Li, J., Wang, Z.,
1245 Donahue, N. M., and Sun, Y.: Organic Aerosol Processing During Winter Severe Haze
1246 Episodes in Beijing, J. Geophys. Res.: Atmos., 124, 10248-10263,
1247 https://doi.org/10.1029/2019jd030832, 2019.
1248 Zhao, M., Zhang, Y., Ma, W., Fu, Q., Yang, X., Li, C., Zhou, B., Yu, Q., and Chen,

https://doi.org/10.5194/acp-2022-194
Preprint. Discussion started: 6 April 2022

1249 L.: Characteristics and ship traffic source identification of air pollutants in China's
1250 largest port, Atmos. Environ., 64, 277-286,
1251 https://doi.org/10.1016/j.atmosenv.2012.10.007, 2013.
1252 Zhou, S., Collier, S., Xu, J., Mei, F., Wang, J., Lee, Y.-N., Sedlacek, A. J.,
1253 Springston, S. R., Sun, Y., and Zhang, Q.: Influences of upwind emission sources and
1254 atmospheric processing on aerosol chemistry and properties at a rural location in the
1255 Northeastern U.S, J. Geophys. Res.: Atmos., 121, 6049-6065,
1256 https://doi.org/10.1002/2015jd024568, 2016.
1257

https://doi.org/10.5194/acp-2022-194
Preprint. Discussion started: 6 April 2022

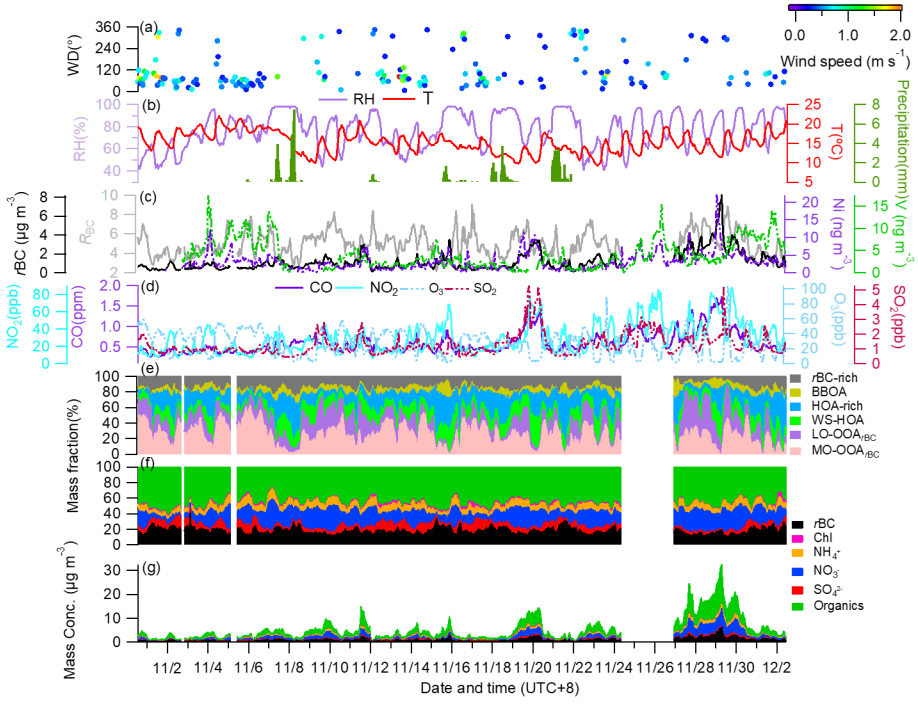

Figure 1. Time series of (a) wind direction (WD) colored by wind speed (WS), (b) air temperature (T), relative humidity (RH) and precipitation, (c) mass concentrations of *r*BC, Ni, V, and R_{BC} (mass ratio of all coating species to *r*BC), (d) mass concentrations of gas pollutants of CO, NO_2, O_3 and SO_2, (e) mass fractions (%) of different OA factors to the total *r*BCc OA, (f) mass fractions (%) of different components to the total *r*BCc mass, and (g) mass concentrations of stacked *r*BCc components.

https://doi.org/10.5194/acp-2022-194
Preprint. Discussion started: 6 April 2022

Atmospheric Chemistry and Physics Discussions

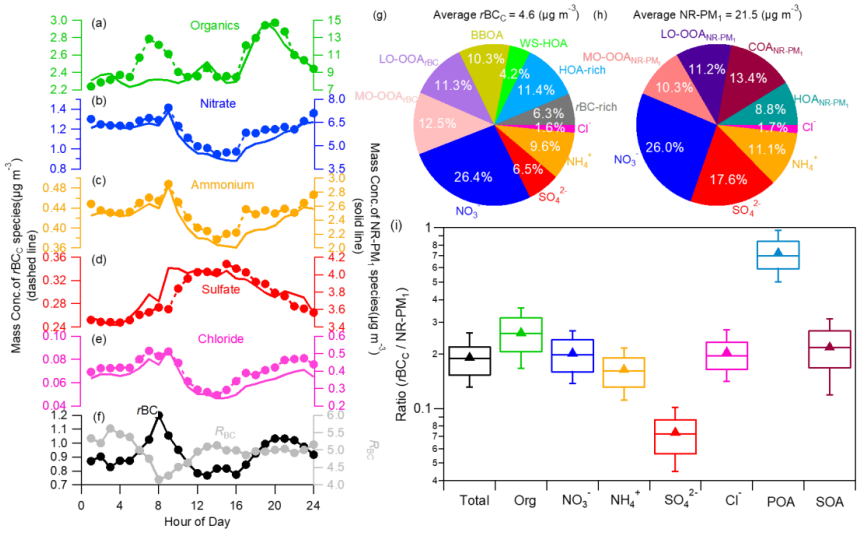

Figure 2. Diurnal cycles of mass concentrations of (a–e) *r*BCc and NR-PM_1 species (organics, nitrate, ammonium, sulfate, and chloride), and (f) *r*BC and R_{BC}. Campaign-average chemical composition of *r*BCc (g) and NR-PM_1 (h). (i) Mass ratios of species in *r*BCc to those in NR-PM_1 (the whiskers above and below the boxes mark the 90% and 10% percentiles, respectively; the upper and lower edge of the boxes represent the 75% and 25% percentiles, respectively; and the lines and triangles inside the boxes denote the median and mean values, respectively; SOA represents ([LO-OOA_{rBC}] + [MO-OOA_{rBC}])/([LO-$OOA_{NR\text{-}PM1}$] + [LV-$OOA_{NR\text{-}PM1}$]), and POA represents ([*r*BC-rich + HOA-rich + BBOA + WS-HOA])/$HOA_{NR\text{-}PM1}$).

https://doi.org/10.5194/acp-2022-194
Preprint. Discussion started: 6 April 2022

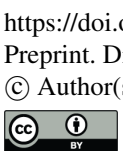

Atmospheric Chemistry and Physics Discussions

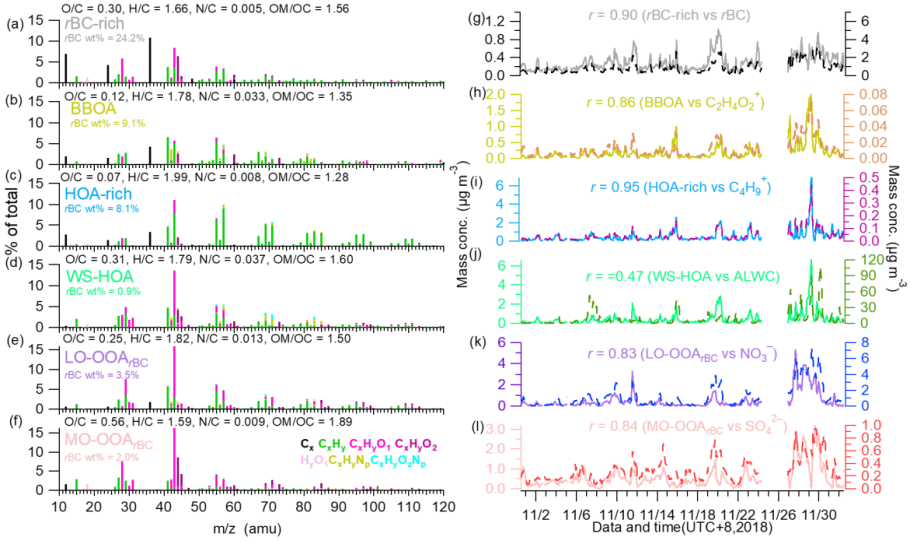

Figure 3. High resolution mass spectra of (a) *r*BC-rich, (b) BBOA, (c) HOA-rich, (d) WS-HOA, (e) LO-OOA$_{rBC}$, and (f) MO-OOA$_{rBC}$. (g-l) Time series of corresponding factors, their tracers (*r*BC, $C_2H_4O_2^+$, $C_4H_9^+$, ALWC, nitrate and sulfate) as well as the correlation coefficients (ALWC refers to aerosol liquid water content, which was estimated by using the extended aerosol inorganic model (Clegg et al., 1998). Calculated ALWC at different RH values is shown in Fig. S4)

https://doi.org/10.5194/acp-2022-194
Preprint. Discussion started: 6 April 2022

Atmospheric Chemistry and Physics Discussions

1283

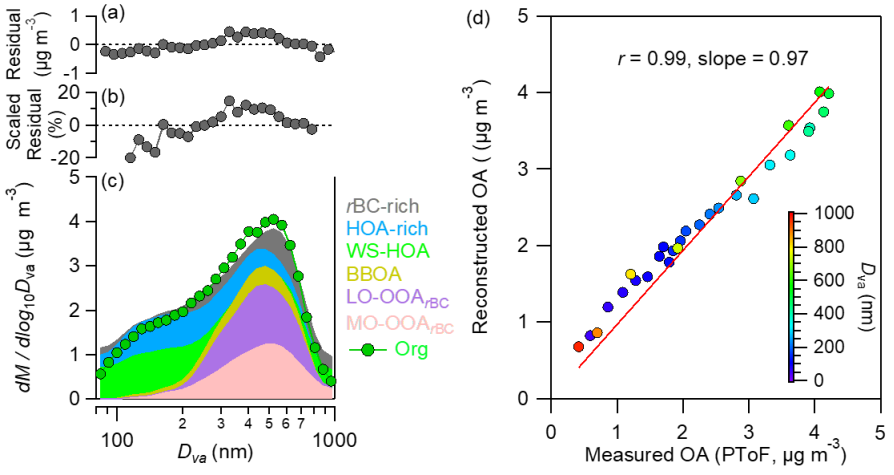

1284

1285 Figure 4. Summary of key diagnostic plots of derivation of size distributions of
1286 individual *r*BCc OA factors. (a) Absolute and (b) relative residuals between the
1287 reconstructed and measured OA mass concentrations in different size bins. (c) Stacked
1288 size distributions of the six OA factors compared to the size distributions of total OA.
1289 (d) Reconstructed OA mass concentrations compared to the measured values for
1290 different size bins (80-1000 nm).

1291

https://doi.org/10.5194/acp-2022-194
Preprint. Discussion started: 6 April 2022

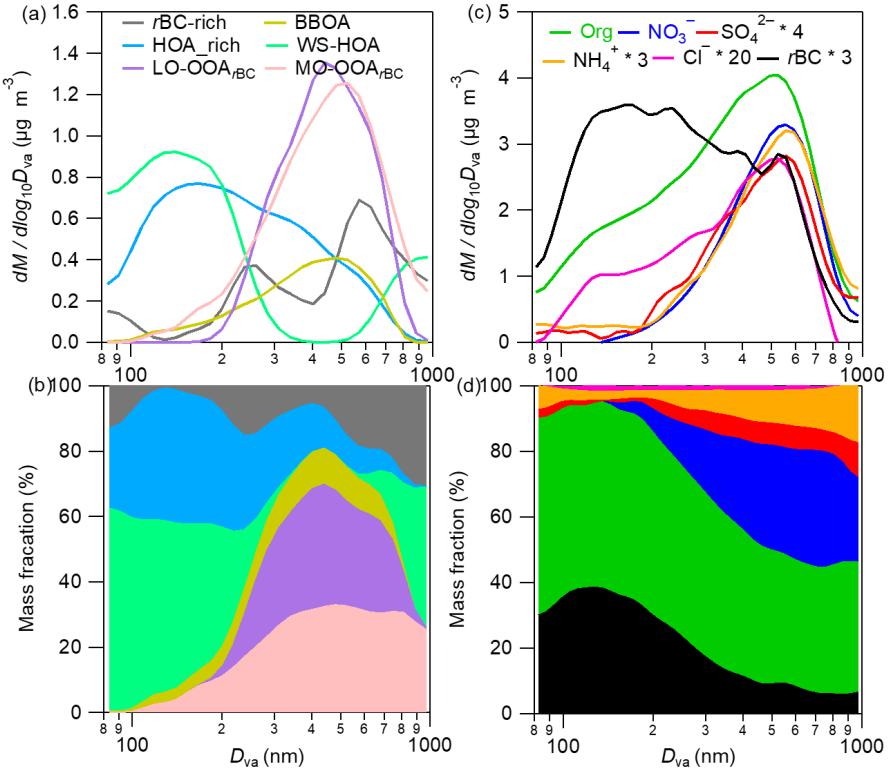

Figure 5. Campaign-average size distributions of six *r*BCc OA factors (a) and individual *r*BCc components (b), and corresponding mass contributions of the six factors to the total *r*BCc OA (c), and the major components to the total *r*BCc (d) at different sizes (80-1000 nm).

https://doi.org/10.5194/acp-2022-194
Preprint. Discussion started: 6 April 2022

Atmospheric Chemistry and Physics Discussions

1298

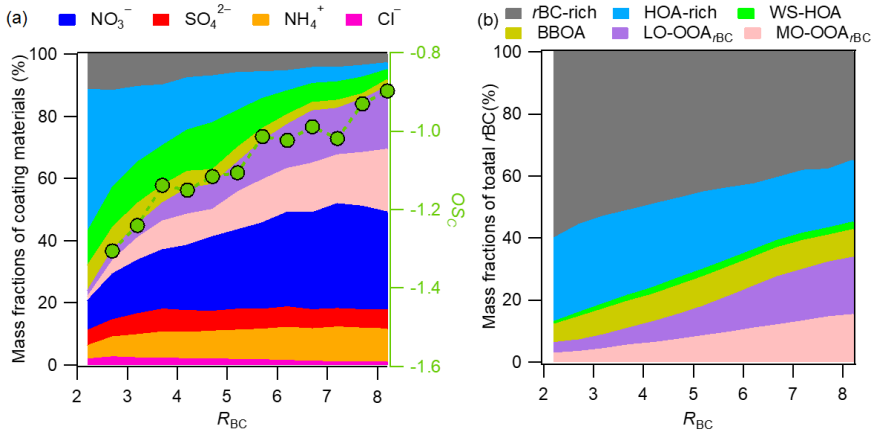

1299

1300 Figure 6. (a) Variations of mass fractions of the major *r*BCc components against R_{BC}.

1301 (b) Variations of mass contributions of individual *r*BCc OA factors to *r*BC against R_{BC}.

1302

https://doi.org/10.5194/acp-2022-194
Preprint. Discussion started: 6 April 2022

Atmospheric Chemistry and Physics Discussions

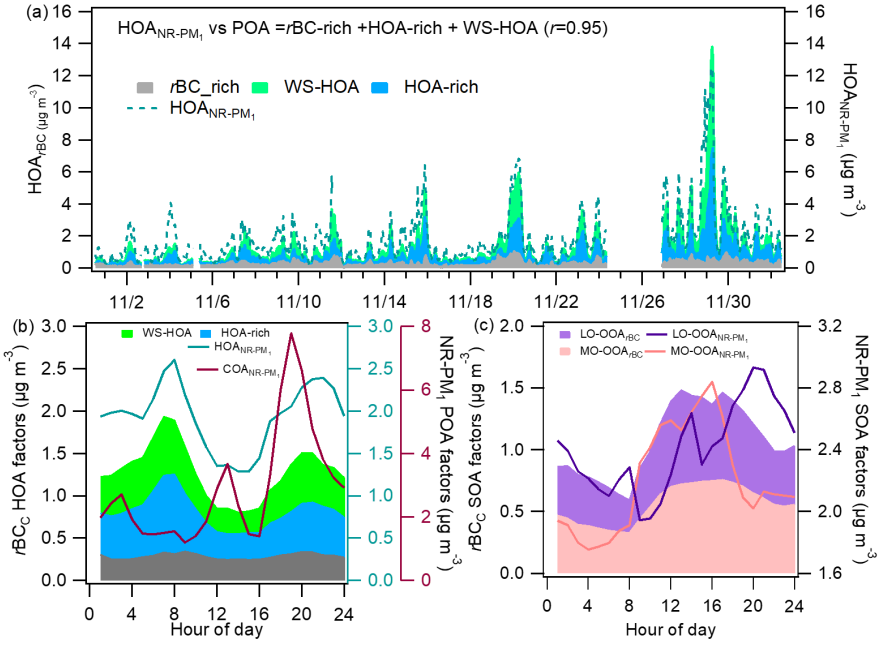

Figure 7. (a) Time series of stacked three rBCc POA factors (i.e., *r*BC-rich, HOA-rich, and WS-HOA) and HOA_{NR-PM1}. Comparisons of the diurnal patterns of different POA factors (b) and SOA factors (c) of *r*BCc and $NR-PM_1$.

https://doi.org/10.5194/acp-2022-194
Preprint. Discussion started: 6 April 2022

Atmospheric Chemistry and Physics Discussions

1308

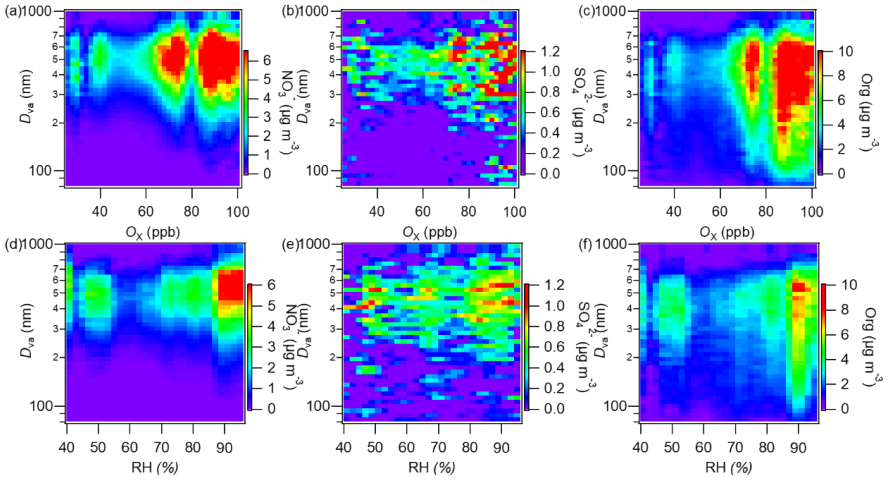

1309

1310 Figure 8. Image plots of size distributions of *r*BCc nitrate, sulfate, organics as a function

1311 of (a-c) Ox and (d-f) RH, respectively (color represents its concentration).

1312

https://doi.org/10.5194/acp-2022-194
Preprint. Discussion started: 6 April 2022

Atmospheric Chemistry and Physics Discussions

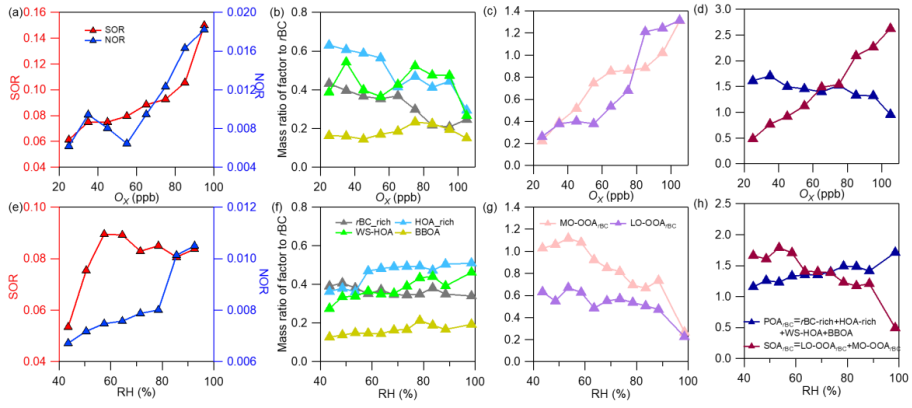

Figure 9. Variations of nitrogen oxidation ratio (NOR) and sulfur oxidation ratio, mass ratios of different POA factors, SOA factors and total POA and SOA to *r*BC against O_X (a-d) and RH (e-h) (NOR= $n\mathrm{NO_3^-}/(n\mathrm{NO_3^-}+n\mathrm{NO_2}+n\mathrm{NO})$ and SOR= $n\mathrm{SO_4^{2-}}/(n\mathrm{SO_4^{2-}}+n\mathrm{SO_2})$, where $n\mathrm{NO_3^-}$, $n\mathrm{SO_4^{2-}}$, $n\mathrm{NO_2}$, $n\mathrm{NO}$ and $n\mathrm{SO_2}$ are the molar concentrations of particle-phase sulfate, nitrate, gaseous $\mathrm{NO_2}$, NO and $\mathrm{SO_2}$, respectively).

https://doi.org/10.5194/acp-2022-194
Preprint. Discussion started: 6 April 2022

Atmospheric Chemistry and Physics Discussions

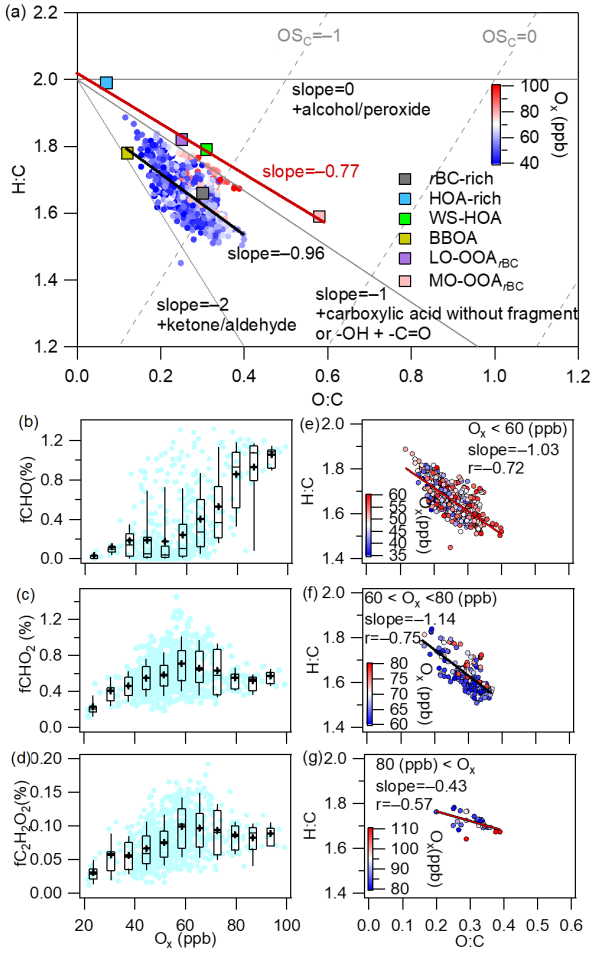

Figure 10. (a) Van Krevelen diagram of H/C versus O/C ratios for all *r*BCc OA and the six factors colored by O_X concentrations (the black line represents the linearly fitted line of all OA data, and the red line is the fitted line of the four OA factors). (b-d) Mass fractions of selected oxygenated ion fragments as a function of O_X (meanings of the boxes are the same as those described in Fig. 2). (e-g) Scatter plots of H/C versus O/C ratios under different O_X levels (data are colored by O_X concentrations).

https://doi.org/10.5194/acp-2022-194
Preprint. Discussion started: 6 April 2022

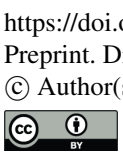

Atmospheric Chemistry and Physics Discussions

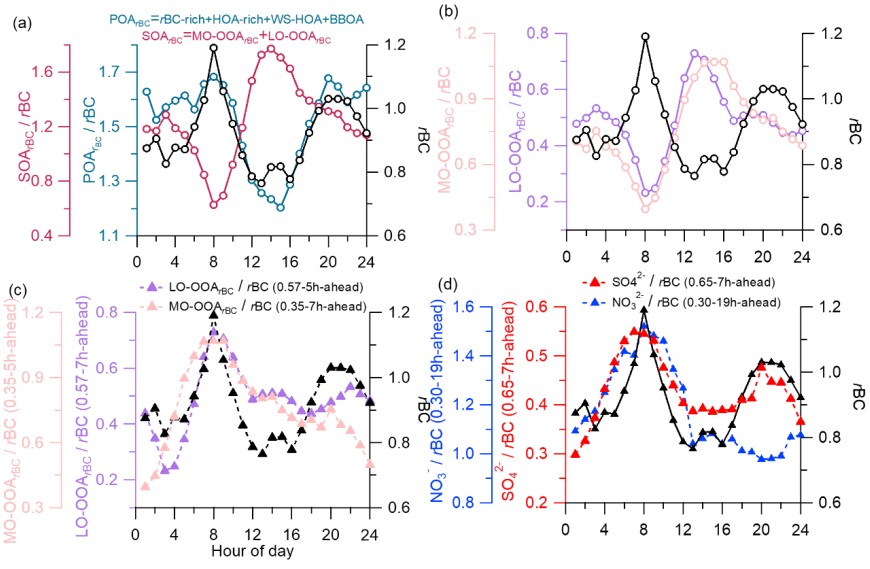

Figure 11. Campaign-average diurnal patterns of (a) *r*BC, POA$_{rBC}$/*r*BC and SOA$_{rBC}$/*r*BC, and (b) *r*BC, MO-OOA$_{rBC}$/*r*BC and LO-OOA$_{rBC}$/*r*BC. Adjusted diurnal patterns by the average coating time (ACT) for (c) LO-OOA$_{rBC}$/*r*BC, MO-OOA$_{rBC}$/*r*BC, and (d) SO_4^{2-}/*r*BC, NO_3^-/*r*BC.

https://doi.org/10.5194/acp-2022-194
Preprint. Discussion started: 6 April 2022

Atmospheric Chemistry and Physics Discussions

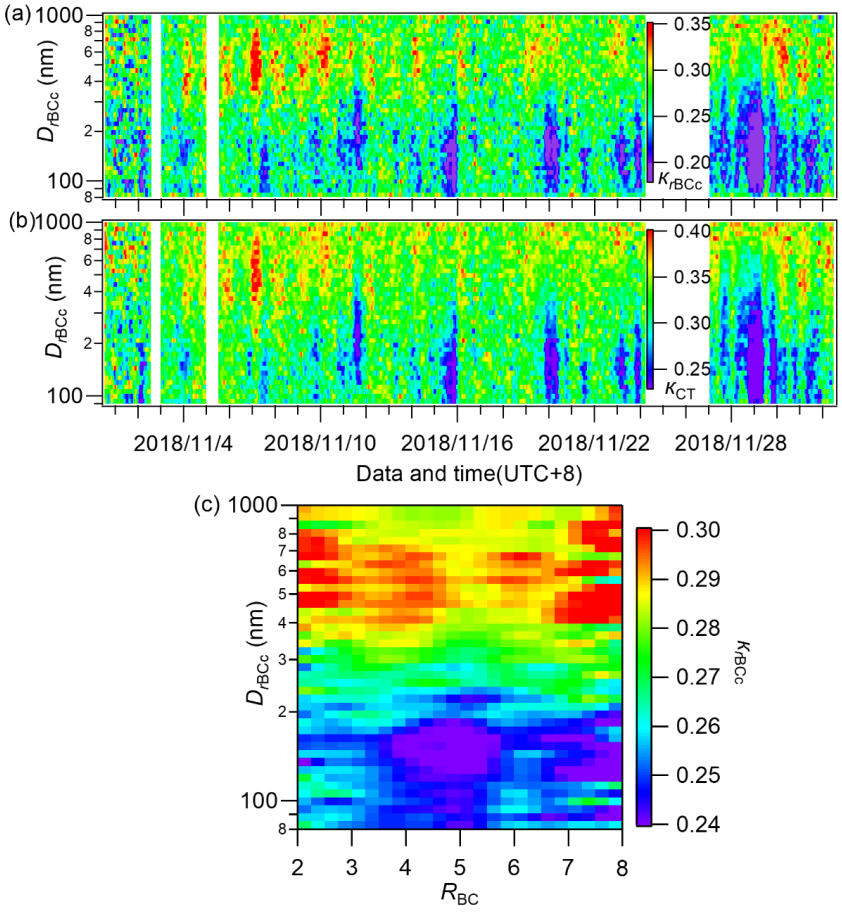

Figure 12. Image plots of size-resolved hygroscopicity parameters of (a) *r*BCc (κ_{rBCc}), (b) its coating materials (κ_{CT}) during the whole campaign, and (c) the campaign-average size-resolved κ_{rBCc} at different R_{BC}.

https://doi.org/10.5194/acp-2022-194
Preprint. Discussion started: 6 April 2022

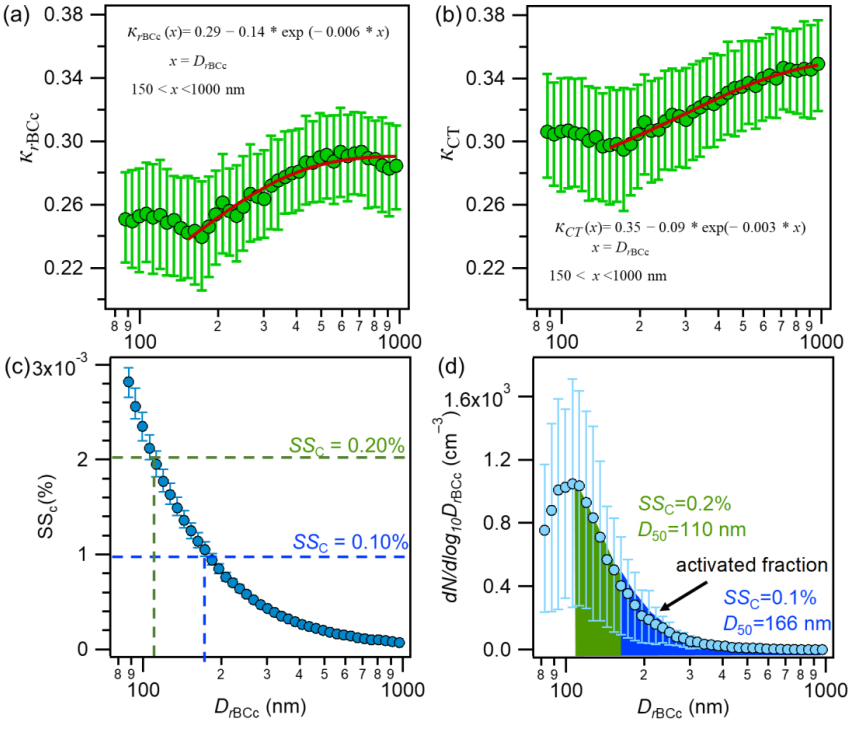

Figure 13. Campaign-average size-resolved hygroscopic parameters for *r*BCc (κ_{rBCc}) and (a) for its coatings (κ_{CT}) (b) (the red lines are exponential fits of the data of 150-1000 nm). (c) Campaign-average size-resolved critical supersaturation (SS_C), and (d) the predicted activated fraction of *r*BCc number concentration based on D_{50} at SS_C of 0.1% (166 nm) and 0.2% (110 nm) (the solid circles are mean values, the upper and lower lines are the 75th and 25th percentiles, respectively).

https://doi.org/10.5194/acp-2022-194
Preprint. Discussion started: 6 April 2022

Atmospheric Chemistry and Physics Discussions

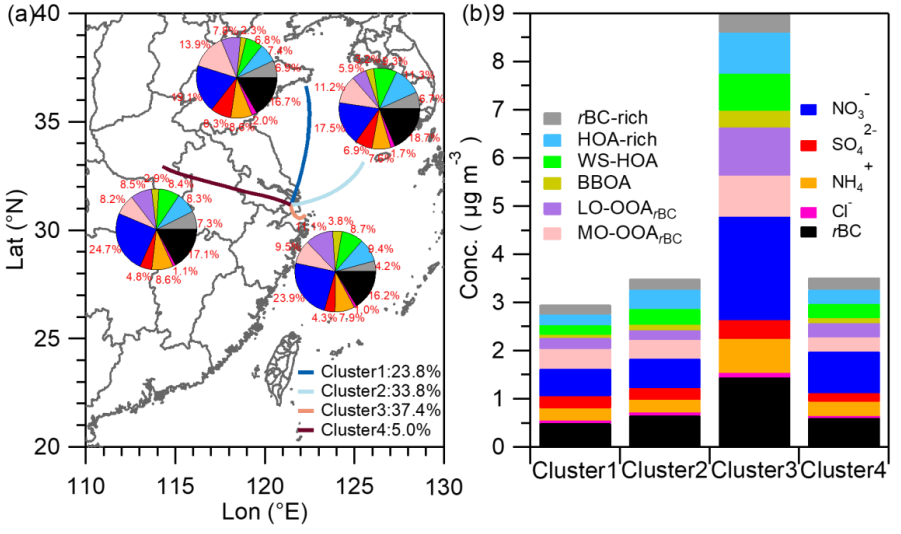

Figure 14. (a) Four clusters of 24-h backward trajectories (at altitude of 500 m) analyzed by NOAA HYSPLIT model (http://www.arl.noaa.gov/ready/hysplit4.html) embedded in Zefir(Petit et al., 2017), with the pie chart showing the average *r*BCc chemical compositions in each cluster. (b) Stacked mass concentrations of the *r*BCc components of the four clusters.

https://doi.org/10.5194/acp-2022-194
Preprint. Discussion started: 6 April 2022

Atmospheric Chemistry and Physics Discussions

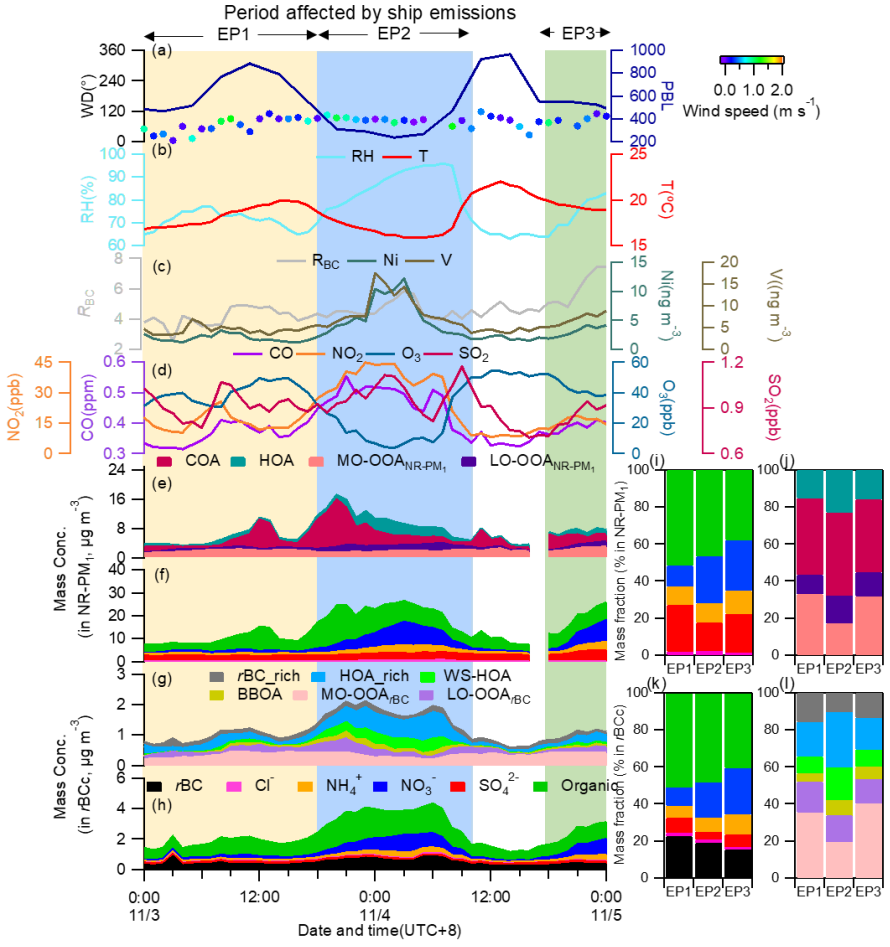

Figure 15. Time series of (a) wind direction (WD) colored by wind speed (WS), planetary boundary layer (PBL) height, (b) relative humidity (RH) and temperature (T), (c) mass concentrations of particle-phase Ni and V, and R_{BC}, (d) mass concentrations of CO, NO_2, O_3, SO_2, stacked concentrations of (e) NR-PM_1 OA factors, (f) NR-PM_1 species, (g) *r*BCc OA factors, and (h) *r*BCc components during the ship emission period (SEP). Mass contributions of different components to NR-PM_1 (i), different OA factors to total NR-PM_1 OA (j), different components to *r*BCc (k), and different OA factors to total *r*BCc OA (l) for the three episodes (EP1, EP2 and EP3).